https://doi.org/10.5194/cp-2020-114
Preprint. Discussion started: 2 October 2020

Climate of the Past Discussions

Deoxygenation dynamics above the western Nile deep-sea fan during sapropel S1 at seasonal to millennial time-scales

Cécile L. Blanchet[1], Rik Tjallingii[1], Anja M. Schleicher[2], Stefan Schouten[3], Martin Frank[4], Achim Brauer[1]

[1] GFZ Potsdam, Department of Climate and Landscape Dynamics, Telegrafenberg, 14743 Potsdam, Germany
[2] GFZ Potsdam, Department of Inorganic and Isotope Geochemistry, Telegrafenberg, 14743 Potsdam, Germany
[3] Royal NIOZ, Department of Marine Microbiology and Biogeochemistry, Landsdiep 4, 1797 SZ 't Horntje, Texel, The Netherlands
[4] GEOMAR, Research Unit Paleoceanography, Wischhofstrasse 1-3, D-24148 Kiel, Germany

Correspondence to: Cécile L. Blanchet (blanchet@gfz-potsdam.de)

https://doi.org/10.5194/cp-2020-114
Preprint. Discussion started: 2 October 2020

Climate of the Past Discussions

12 **Abstract**

13 Ocean deoxygenation is a rising threat to marine ecosystems and food resources under present climate warming
14 conditions. Organic-rich sapropel layers deposited in the Mediterranean Sea provide a natural laboratory to study
15 the processes that have controlled the changes in seawater oxygen levels in the recent geological past. Our study is
16 based on three sediment cores spanning the last 10 thousand years (10 kyr BP) and located on a bathymetric transect
17 offshore the western distributaries of the Nile delta. These cores are partly to continuously laminated in the sections
18 recording sapropel S1, which is indicative of bottom-water anoxia above the western Nile deep-sea fan. We used a
19 combination of microfacies analyses and inorganic and organic geochemical measurements to reconstruct changes
20 in oxygenation conditions at seasonal to millennial time-scales. The regular alternations of detrital, biogenic and
21 chemogenic sublayers in the laminated sequences are interpreted in terms of seasonal changes. Our microfacies
22 analyses reveal distinct summer floods and subsequent plankton blooms preceding the deposition of inorganic
23 carbonates formed in the water-column during spring-early summer. The isotopic signature of these carbonates
24 suggests year-round anoxic to euxinic bottom waters resulting in high levels of anaerobic remineralisation of
25 organic matter and highlights their potential to reconstruct seawater chemistry at times when benthic fauna was
26 absent. Synchronous changes in terrigenous input, primary productivity and past oxygenation dynamics on
27 millennial time-scales obtained by our multi-proxy study show that runoff-driven eutrophication played a central
28 role in driving rapid changes in oxygenation state of the entire Levantine Basin. Rapid fluctuations of oxygenation
29 conditions in the upper 700 m water depth occurred above the Nile deep-sea fan between 10 and 6.5 ka BP while
30 deeper cores recorded more stable anoxic conditions. These findings are further supported by other regional records
31 and reveal time-transgressive changes in oxygenation state driven by rapid changes in primary productivity during
32 a period of long-term deep-water stagnation.

35 **1 Introduction**

36 The present-day Mediterranean Sea is well-oxygenated due to a vigorous thermohaline circulation of intermediate-
37 and deep-water initiated in the eastern part of the basin (Pinardi et al., 2015; Roether et al., 1996). However,
38 recurring episodes of water-column stratification and severe oxygen depletion have been recorded in Mediterranean
39 sediments (Cramp and O'Sullivan, 1999; Rossignol-Strick, 1985). These episodes marked by sapropel deposits
40 were caused by drastic modifications of the sea-surface hydrological balance (Rohling, 1994). Orbital-forced

https://doi.org/10.5194/cp-2020-114
Preprint. Discussion started: 2 October 2020


Climate of the Past Discussions

enhancement of monsoonal precipitation over North Africa led to high freshwater discharge into the Eastern Mediterranean (mostly through the Nile River) and generated large-scale perturbations of the Mediterranean thermohaline circulation (Rohling et al., 2015). Seawater freshening is also a well-known perturbator in the North Atlantic that has led to slowing down or even complete shutting down of Atlantic Meridional Overturning Circulation during the last glacial period (Ganopolski and Rahmstorf, 2001). In the Mediterranean Sea, the input of relatively low-saline Atlantic seawater also exerted a large control on deep-water ventilation (Rogerson et al., 2012). The inflow of Atlantic-derived seawater at the Gibraltar Strait as early as 16-17 ka BP during deglacial sea-level rise decreased the buoyancy of surface waters and led to long-lasting deep-water stagnation in the eastern Mediterranean (Rogerson et al., 2010), which is seen as a pre-condition for the development of basin-scale anoxia during sapropel S1 (11-6 ka BP) (Cornuault et al., 2018; Grimm et al., 2015).

A specificity of the eastern Mediterranean lies in its current nutrient-limitation and the consequently low or quasi-absent primary productivity (Krom et al., 2014). Nutrient-poor surface waters are advected from the western to the eastern Mediterranean and riverine nutrients (e.g. discharged by the Nile River) are quickly utilized or extracted by intermediate water circulation flowing westward (Fig. 1a). Prior to the construction of the Aswan Dam in 1965, the surface waters in the Levantine basin were seasonally fertilised by riverine nutrient input during the summer Nile floods (Halim et al., 1967). These so-called “Nile Blooms” of phytoplankton sustained traditional fisheries of sardines and prawns (Nixon, 2003). After 1965, the Nile River discharge was reduced by 90% and thereby largely annihilated the main nutrient source to the eastern Mediterranean, initiating the present-day ultra-oligotrophic conditions. Since the 1980’s however, the transition from a flood-sustained to a fertiliser-sustained agriculture in the Nile valley has led to a larger release of nutrients by the Nile River, which boosted primary productivity and renewed the fish stocks (Nixon, 2003). Anthropogenic fertilisation processes in coastal waters might have potential adverse effects as well, such as water deoxygenation or harmful algal blooms (Nixon, 2003). Eutrophication and severe anoxia due to anthropogenic fertilisation have been indeed observed in semi-enclosed settings such as the Baltic Sea (Jilbert and Slomp, 2013). In this context of increasing nutrient loading, it is crucial to estimate the changes in intermediate and deep-water ventilation caused by climate change. Modelling experiments predict a temperature and salinity rise for the Mediterranean over the next decades, which overall will result in a weakening of the thermohaline circulation in the Mediterranean (e.g., Somot et al., 2018). Sensitivity simulations showed that hypoxia might develop in the Mediterranean as a result of reduced deep ventilation over long time scales (>1000 yr) (Powley et al., 2016). Although basin-wide oxygen depletion is unlikely to develop as a result of the 21rst century climate change, the predicted changes in O_2 distributions do not account for additional factors that may affect O_2 consumption rates, in particular, rising inputs of anthropogenic nutrients (Powley et al., 2016).

https://doi.org/10.5194/cp-2020-114
Preprint. Discussion started: 2 October 2020


Climate of the Past Discussions

Sapropels have proven a valuable laboratory to investigate the complex interplay between oceanographic, hydrological and biogeochemical processes driving Mediterranean deoxygenation (Rohling et al., 2015; Rossignol-Strick et al., 1982). Here we present a set of unique sediment cores retrieved along a bathymetric section near the main western Nile tributary, the Rosetta channel, to investigate the relationships between terrigenous inputs, primary productivity, and the development of sub- to anoxic conditions in intermediate water masses. The location of our study site close to the mouth of the Nile River allows to reconstruct changes in fluvial nutrient supply and associated fertilisation of the marine ecosystem.

2 Regional context

Surface waters originating from the North Atlantic flow into the Levantine Basin (Pinardi et al., 2015), which gradually become more saline due to evaporation as they flow eastwards in the Mediterranean Sea (Fig. 1a). Elevated salinity of surface waters in the eastern Levantine Basin (ca. 39 PSU) (MEDAR Group, 2002) in combination with cooler temperatures in winter lead to high surface water density and formation of the Levantine intermediate water (LIW), which flows westwards at water depths between 200 and 500 m (Cornuault et al., 2018; Pinardi et al., 2015). Deeper water masses flow below the LIW and form by incorporation of cold surface waters from the Adriatic Sea and sometimes dense waters from the Aegean Sea to the LIW (Cornuault et al., 2018; Robinson et al., 1992; Roether et al., 2007).

The main source of freshwater to the Levantine Basin is the Nile River runoff through the active Rosetta channel located in the western part of the Nile Delta (Fig. 1). Although the present Nile flow is drastically reduced compared to historical times (Halim et al., 1967), runoff still leads to marked salinity gradients (halocline) in the upper 200 m water-depth (w-d), in particular during the summer monsoon (Fig. 1a).

Table 1. Sediment cores used for the present study, with names used throughout the paper, water-depths and coordinates.

Core Name	Shortened	Water-depth (m)	Latitude (dec. deg.)	Longitude (dec. deg)
P362/2-33	P33	738	31.700	29.768
P362/2-73	P73	569	31.987	30.156
P362/2-99	P99	396	31.953	30.160

https://doi.org/10.5194/cp-2020-114
Preprint. Discussion started: 2 October 2020

Climate of the Past Discussions

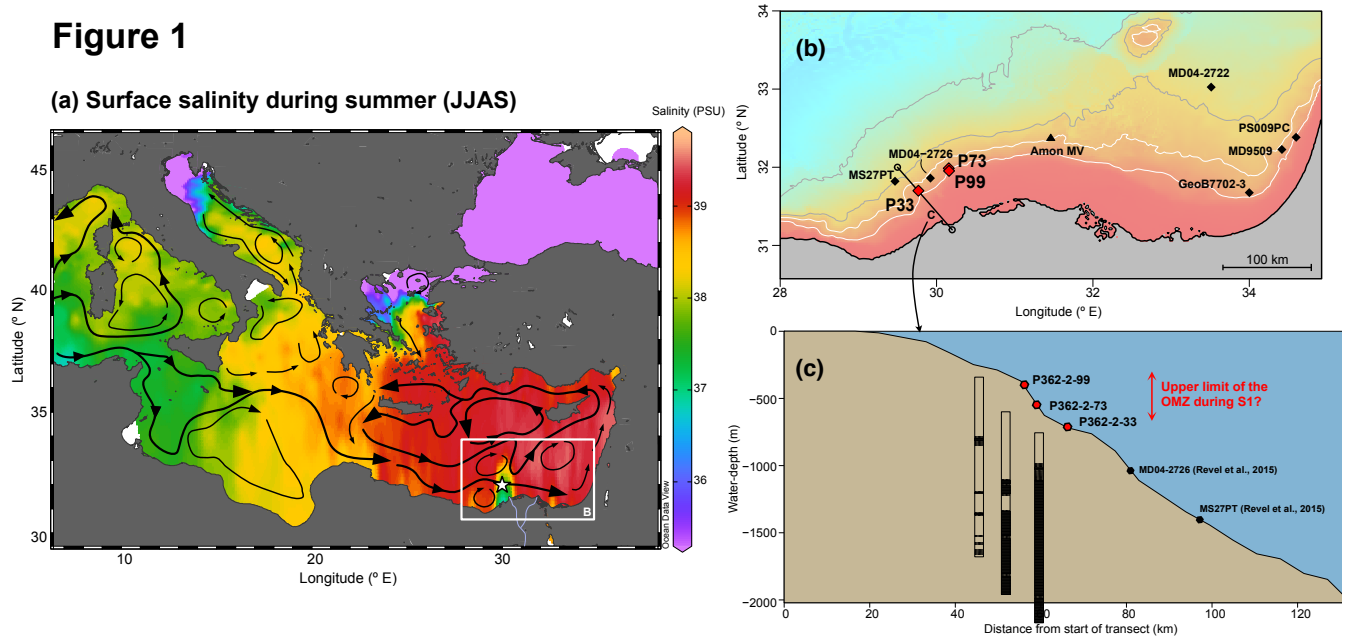

Figure 1. Regional context and location of the cores. (a) Sea-surface salinity during the summer months (June to September) (MedAtlas, MEDAR Group, 2002) plotted with the Ocean Data View software (Schlitzer, 2018). White star: location of the Nile River freshwater plume. Black arrows: surface currents redrawn ((Pinardi et al., 2015; Rohling et al., 2015). (b) Zoom on the western Nile deep-sea fan (DSF), with locations of cores P33, P73 and P99, as well as neighbouring cores MS27PT and MD04-2726 (Revel et al., 2015), MD04-2722 (Tachikawa et al., 2015), GeoB7702-3 (Castañeda et al., 2010), PS009PC (Hennekam et al., 2014), MD9509 (Matthews et al., 2017) (black diamonds) and the Amon mud volcanoe (black triangle). White contours: 500-m and 1000-m isobaths and grey contours: 1500-m and 2000-m isobaths. (c) Bathymetric transect across the western Nile DSF with sediment lithological features (black: laminations and stripes: faint laminations). Map and bathymetric transect in (a) and (b) plotted using the R freeware (R Core Team, 2013), the marmap package (Pante and Simon-Bouhet, 2013) and gridded bathymetric data from Gebco (Gebco team, 2014).

3 Material and methods

3.1 Sediment cores

For our study, we use three gravity cores that were retrieved during the oceanographic campaign P362/2 "West Nile Delta" onboard the R.V. Poseidon in August 2008 (Feseker et al., 2010) (Table 1). These sediment cores are located along a bathymetric section on the western Nile deep-sea fan (DSF), in the vicinity of the North Alex and Giza mud volcanoes (Feseker et al., 2010) (Fig. 1b,c). Cores P362/2-73 (P73) and P362/2-99 (P99) are located close to each other and ca. 75 km eastward of core P362/2-33 (P33), on the opposite side of the submarine Rosetta canyon (Fig. 1b). Core P33 was recovered at 738 m water-depth, is 5.6 m-long and contains well-preserved mm-scale laminations in the lower 5 m of the core (see Blanchet et al., 2013, 2014, for detailed descriptions) (Fig. 1c,

https://doi.org/10.5194/cp-2020-114
Preprint. Discussion started: 2 October 2020

Climate of the Past Discussions
Open Access
EGU

2). Core P73 was collected at 569 m depth, is 5.4 m-long and contains an alternation of finely laminated (similar to P33) and bioturbated intervals (Fig. 1c, 2). Core P99 is located at 396 m depth, is 5.3 m-long and contains a few laminated intervals within otherwise bioturbated sediments (Fig. 1c, 2). All cores are composed of clay-rich dark-brown hemipelagic mud, which shows significantly lighter colours in the upper 1m of the cores. In cores P33 and P73, several harder carbonate-rich layers were identified (Fig. 2).

A qualitative assessment of the foraminiferal assemblage was realised in the lower part of core P33 (between 75 and 558 cm), with a particular emphasis on benthic foraminifera. Following assessments by previous authors for the eastern Mediterranean (Abu-Zied et al., 2008; Jorissen, 1999; Schmiedl et al., 2003), we identified epifaunal species *Planulina* spp. and *Cibbides* spp., shallow infaunal species *Bolivina/Brizalina* spp. and *Uvigerina* spp. And deep infaunal species *Globobullimina* spp. and *Chillostomella* spp.

Table 2: Radiocarbon ages, tie-points and modelled ages for cores P33, P73 and P99. Radiocarbon ages for core P33 from Blanchet et al. (2013), with new modelled ages with uncertainties for the entire core (using Bacon V2.3, Blaauw and Christen, 2011). Six tie points were defined on the Ti/Ca record of P33 (T1 to T6, see sect. 3.2 and Fig. 2). New radiocarbon measurements, tie-points and modelled ages with uncertainties for cores P73 and P99. Pk: planktonic, Bk: benthic foraminifera.

Sample name	Depth (cm)	material	14C age ± 1σ	C cont. (mg)	DeltaR ± 1σ	Calib curve	cal. age BP ± 2σ	modelled median age (Bacon)
P362/2-33 (P33)								
	1.5±1.5	Steamboat cinders					75±75	161± 210
KIA 38572	30±0.5	Pk foraminifera	3825±30	1.3	0	Marine13	3775±100	3840±180
KIA 38573	50±0.5	Pk foraminifera	5695±30	1.3	0	Marine13	6110±100	6140±150
KIA 38574	75±0.5	Pk foraminifera	6855±35	1.6	150±30	Marine13	7235±105	7260±180
KIA 37800	100±0.5	Pk foraminifera	7340±45	1.2	150±30	Marine13	7655±110	7825±150
KIA 38575	152±2.5	Pk foraminifera	7920±45	1.3	150±30	Marine13	8240±120	8165±130
KIA 37801	200±0.5	Pk foraminifera	8115±55	1.1	150±30	Marine13	8430±125	8405±120
KIA 38576	252±2.5	Pk foraminifera	8360±40	1.1	150±30	Marine13	8725±180	8610±115
KIA 37802	300±0.5	Pk foraminifera	8375±60	0.9	150±30	Marine13	8750±200	8765±110
KIA 38577	327±3	Pk foraminifera	8495±35	1.3	150±30	Marine13	8925±160	8850±110
KIA 37803	399±1	Pk foraminifera	8440±45	1.4	150±30	Marine13	8845±175	9050±105
KIA 38578	463±2	Pk foraminifera	8680±40	1	150±30	Marine13	9165±150	9280±100
KIA 37804	499±1	Pk foraminifera	8805±45	1.5	150±30	Marine13	9330±145	9410±100
KIA 38579	547±3	Pk foraminifera	9010±35	1.2	150±30	Marine13	9515±100	9595±125
KIA 37805	557±1	Pk foraminifera	8780±50	0.7	150±30	Marine13	9300±160	9635±135

https://doi.org/10.5194/cp-2020-114
Preprint. Discussion started: 2 October 2020

Climate of the Past Discussions

T1	8							1000±440
T2	17.5							2250±520
T3	31.5							4030±150
T4	48							5965±140
T5	80.5							7385±110
P362/2-73 (P73)								
Poz-113950	15 ±1	Pk foraminifera + pteropod	505±30	0.9	0	Marine13	130 ±90	80 ±180
T1	18.5						1000±440	265 ±335
T2	47						2250±520	1665±535
Poz-112951	74 ±1	Pk foraminifera	2925±35	0.7	0	Marine13	2710±85	2720±170
T3	85.5						4030±150	3785±500
T5	172						7385±110	7140± 27
Poz-112952	189 ±1	Pk foraminifera	6860±50	>1	150±30	Marine13	7240±130	737 ±170
Poz-113951	473 ±1	Pk + Bk foraminifera	13910±180	0.04	Too little carbon retrieved			
T6	268.5						7700±115	7810±195
P362/2-99 (P99)								
Poz-112947	11 ± 1	Pk foraminifera	415 ±30	0.8	0	Post-bomb curve NHZ2	80 ±15	40 ±135
T1	31.5						1000±440	1150±615
T2	54.5						2250±520	2590±800
T3	73.5						4030±150	4255±920
Poz-112948	79 ±1	Pk foraminifera	5990±50	>1	0	Marine13	6400±120	5250±960
T4	91						5965±140	6155±620
T5	112						7385±110	7170±285
Poz-112949	322 ±2	Pk foraminifera	7890±60	0.5	150±30	Marine13	8210±150	8200±190
Poz-112950	518 ±1	Pteropod	8390±60	>1	150±30	Marine13	8770±200	9070±275

3.2 Age determination and transformation depth-to-age

The chronology of core P33 has been constructed based on a set of 14 radiocarbon samples (Blanchet et al., 2013). We prepared another 8 samples for radiocarbon dating using planktonic foraminifera and pteropod shells, which provide tie-points for cores P73 and P99 (Table 2). Only one sample in core P73 (Poz-113951) did not generate

https://doi.org/10.5194/cp-2020-114
Preprint. Discussion started: 2 October 2020

137 enough carbon for an accurate dating. The new radiocarbon measurements were performed at the Poznan
138 radiocarbon laboratory (Poland).
139 More detailed stratigraphic constrains were obtained from correlation of the titanium over calcium (Ti/Ca) records
140 of cores P73 and P99 with core P33 (Fig. 2). It was shown that changes in sedimentation rates are coherent on the
141 western Nile DSF (Hennekam et al., 2015) and Ti/Ca records show similar patterns (Fig. S1). Six tie-points (marked
142 T1-T6 on Fig. 2) mark changes in Ti/Ca records identified in the upper parts of the cores and were used to further
143 synchronise the records of P73 and P99 with core P33 (Table 2).
144 The age-depth modelling was performed using Bacon version 2.3 (Blaauw and Christen, 2011), which enables to
145 discriminate between sections of the core with contrasting accumulation rates and to provide these as priors.
146 Convergence and mixing of the Markov chain Monte Carlo iterations used to build the age model by Bacon was
147 tested and the number of iterations was adjusted to obtain a Gelman and Rubin Reduction factor below 1.05
148 (Blaauw and Christen, 2011; Brooks and Gelman, 1998). The new age-depth model of core P33 based on
149 radiocarbon ages is similar to that presented in Blanchet et al. (2013), but age uncertainties are now available for
150 the whole core (Table 2 and Fig. 2a). Radiocarbon ages and the six tie-points were used for age modelling for cores
151 P73 and P99 using the Bacon program following a similar procedure to that used for core P33 (Blaauw and Christen,
152 2011). For the lowest part of core P73, for which there is no tie-point, we evaluated the ages and uncertainties using
153 the range of sedimentation rates observed in the other two cores for ages older than 7500 years and derived the
154 median sedimentation rate applying the maximum and minimum sedimentation rates observed as uncertainty range
155 (Fig. 2).
156

https://doi.org/10.5194/cp-2020-114
Preprint. Discussion started: 2 October 2020

Climate of the Past Discussions

Figure 2

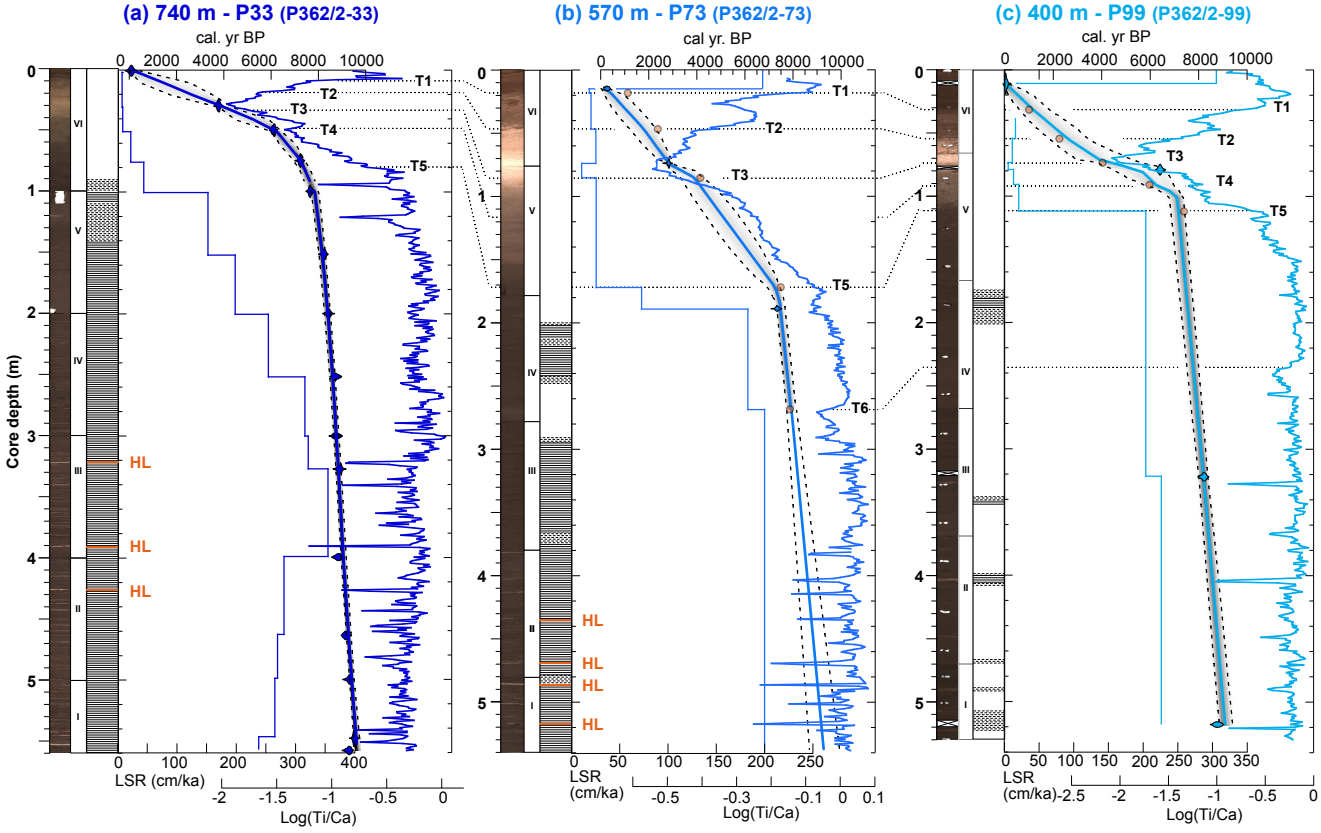

Figure 2. Age models. (a) core P33, (b) core P73 and (c) core P99. For all cores, from left to right: core depth (m), half-core surface images (for core P99, realised after sampling with empty sections shown as crosses), section number (roman numbers), schematic lithological log (white: bioturbated, dashed: faint laminations, hatched: laminations, orange: hard layers labelled HL), linear sedimentation rates (cm/ka, step curves), age-depth relationships as computed by Bacon V2.3 (Blaauw and Christen, 2011) with radiocarbon ages (blue violin distributions) and tie points (orange dots), Log(Ti/Ca) records with tie-points T1-T6 (dashed lines) (Tab. 2).

3.3 Microfacies description and scanning electron microscopy

A detailed examination of the microfacies was performed on the laminated part of core P33 (i.e., between 100 and 559 cm) and on a few samples of cores P73 and P99. Sediment blocks of 10 cm-long, 2 cm-wide and 1 cm-thick were cut out of the fresh sediment with 2-cm overlaps to enable continuous microfacies analysis. Preparation of thin-sections from soft and wet sediment blocks followed a standard procedure minimizing process-induced disturbances of sediment micro-structures and included shock-freezing with liquid nitrogen, freeze-drying for 48 h, and epoxy resin impregnation under vacuum (Brauer and Casanova, 2001).

https://doi.org/10.5194/cp-2020-114
Preprint. Discussion started: 2 October 2020


Climate of the Past Discussions

Detailed microfacies analysis was performed on the overlapping series of large-scale petrographic thin sections. Microscopic analysis included the investigation of sediment using a petrographic microscope with non-polarized and (cross)-polarized light, at 5x–40x magnifications (Carl Zeiss Axioplan). Backscatter scanning electron microscope (SEM) images and energy dispersive spectroscopy (EDS) elemental analyses were acquired at GFZ Potsdam using a Phenom™ XL. SEM and EDS analyses were performed on dried power samples mounted on a graphite coated sample holder.

3.5 Mineralogy

The mineralogical composition was determined by X-ray diffractometry (XRD) on random powder samples of core P33. Therefore, the rock chips were powdered to a grain size of < 63 µm, and loaded from the back side of the sample holders. XRD analyses were performed with a PANalytical Empyrean x-ray diffractometer operating with Bragg-Brentano geometry at 40 mA and 40 kV with CuKα radiation and PIXel3D detector at a step size of 0.013 °2θ from 4.6 to 85 °2θ and 60 sec per step. The Mineralogy was determined qualitatively with the EVA software (version 11.0.0.3) by Bruker.

3.4 X-Ray Fluorescence scanning

The bulk sediment compositions for cores P33 and P99 were measured using an Aavatech^{TM} X-Ray fluorescence (XRF) core-scanner at the Institute of Geosciences of the University of Kiel (Germany) (Table S1 and S2). Non-destructive XRF core-scanning measurements were performed every 1 cm using a Rh X-Ray source at 10 kV and 0.65 mA to acquire the elements S, Cl, K, Ca and Ti. Core P73 was measured using an ITRAX XRF core-scanner at GFZ Potsdam (Germany) (Table S3). These measurements were conducted every 1 cm with a Cr- X-Ray source operated at 30 kV and 60 mA to cover the same elements as acquired for core P33 and P99. Element intensity records obtained by XRF core-scanning are susceptible to down-core variations of physical properties, sample geometry and non-linear matrix effects (Tjallingii et al., 2007). These effects can be minimized by log-ratio transformation of element intensities, which also provide the most easily interpretable signals of relative changes in chemical composition (Weltje et al., 2015; Weltje and Tjallingii, 2008).

Two epoxy embedded samples of core P33 that are representative for the fine (P33-5 77-87 cm) and thick (P33-2 59-69 cm) laminations have been selected for µ-XRF element mapping. Measurements are conducted every 50 µm at 50 kV, 600 µA and 50 ms using a Bruker M4 Tornado, which is equipped with a Rh X-ray source in combination with poly-capillary X-ray optics generating an irradiation spot of 20 µm. Mapping results of the element K, Ca, and Ti representing solid-state chemical components are presented as normalized element intensities after initial

https://doi.org/10.5194/cp-2020-114
Preprint. Discussion started: 2 October 2020


Climate of the Past Discussions

spectrum deconvolution (Fig. 3). However, elements that occur predominantly in pore fluids (e.g. Cl and S) are not well preserved in epoxy embedded samples.

3.6 Stable oxygen and carbon isotopes

Measurements of stable oxygen and carbon isotopes were realized both at GEOMAR and GFZ (Table S4). Carbonate-rich layers were sampled individually and all samples were subsequently freeze-dried and carefully ground. In order to dissolve only the carbonates in the powdered samples, we used orthophosphoric acid at 70 ℃ in a Kiel II (GEOMAR) or Kiel IV (GFZ-Potsdam) carbonate device. The CO_2 released was analysed using a Thermo Scientific MAT 252 (GEOMAR) or MAT 253 (GFZ-Potsdam) isotope ratio mass spectrometer (IRMS). The oxygen and carbon isotopic composition were calibrated against international limestone standard (NBS 19) and are reported relative to the Vienna Peedee Belemnite (VPBD) in the delta notation. Analytical precision of 0.06 ‰, for both the $\delta^{18}O$ and $\delta^{13}C$ measurements, were determined from repeated analyses of internal limestone standards.

3.7 Biomarkers

All biomarkers (tetraether lipids, *n*-alkanes and alkenones) were measured at the organic geochemistry laboratory of NIOZ (Texel, Netherlands) on cores P33 and P99 (Table S5 and S6). The lipids were extracted from 63 sediment samples with a DIONEX Accelerated Solvent Extractor 200 at the NIOZ using a solvent mixture of 9:1 (v/v) dichloromethane (DCM)/methanol (MeOH). After addition of internal standards C_{22} anti-isoalkane (*n*-alkanes), 10-nonadecanone (alkenones) and C_{46} glycerol trialkyl glycerol tetraether (GDGTs), the total lipid extract was separated into apolar, ketone and polar fractions using pipette column chromatography loaded with aluminium oxide and the solvent mixtures 9:1 (v/v) hexane/DCM, 1:1 hexane/DCM and 1:1 DCM/MeOH as eluents, respectively. The apolar fraction was then separated into saturated hydrocarbon (long-chain odd *n*-alkanes and the C_{22} anti-iso standard) and aromatic fractions using pipette columns loaded with Ag^+-impregnated silica and hexane and ethylacetate as eluents, respectively.

https://doi.org/10.5194/cp-2020-114
Preprint. Discussion started: 2 October 2020

Climate of the Past Discussions
Open Access
EGU

Figure 3

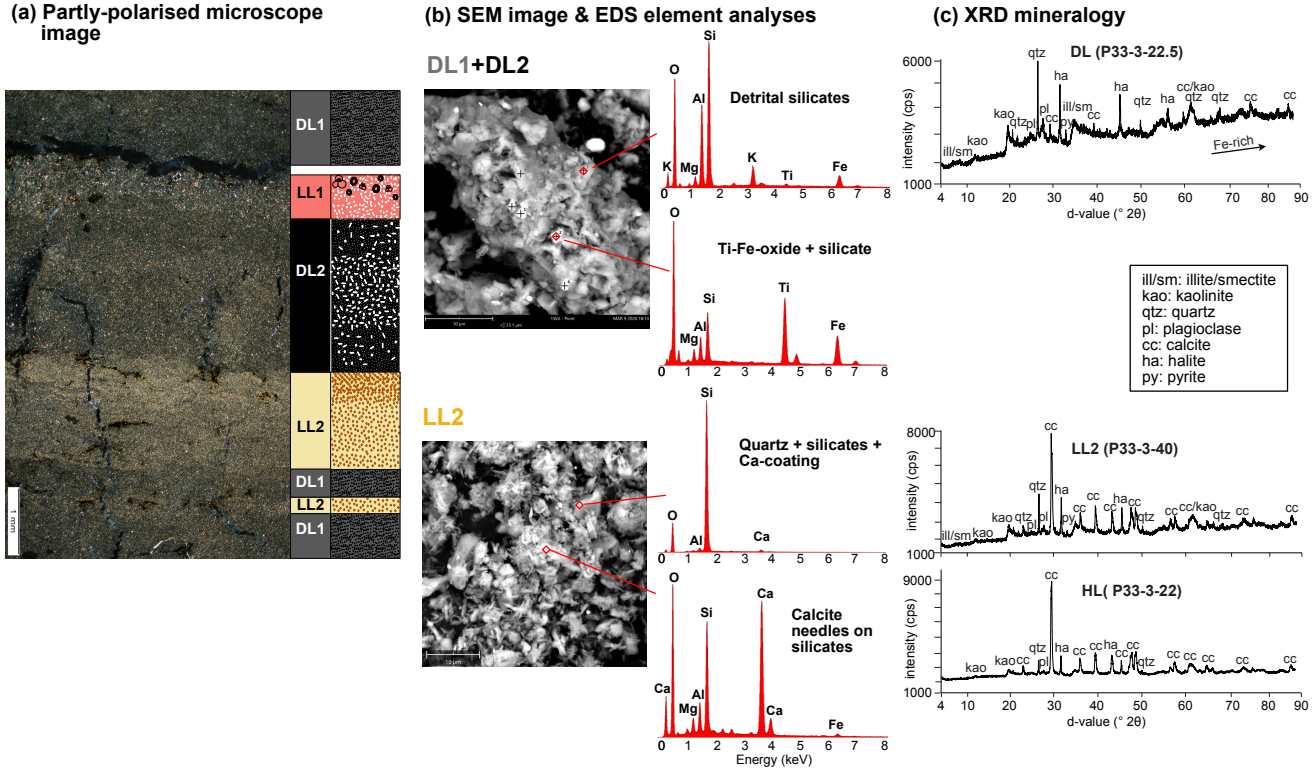

Figure 3. Microscopic, elemental and mineralogical characterisation of sublayers. (a) Micro-facies and mineralogy of a typical sublayer succession in cores P33 and P73. Left to right: part-polarized microscope image and schematic log of sublayers succession DL1-LL2-DL2-LL1. (b) SEM images of powdered dark (DL1+DL2) and light sublayers (LL2) with EDS elemental identification. (c) mineralogical assemblage of powdered DL, LL and HL samples using XRD scans (from 4 to 85 °2θ). In sample DL (P33-3-22.5), the increase of the intensity baseline towards higher angles is due to the presence of an Fe-rich phases, probably pyrite.

Molecular identification of the alkenones and *n*-alkanes was performed on a Thermo Finnigan Trace Gas Chromatograph (GC) Ultra coupled to a Thermo Finnigan DSQ mass spectrometer (MS). The alkenones and the *n*-alkanes were quantified with gas chromatography coupled to flame ionization detection. For GC analysis we used an Agilent HP 6890 GCs with CP Sil-5 columns (50 m length for the alkenones and 25 m for the *n*-alkanes) and helium as the carrier gas. Within the saturated hydrocarbon fraction, we also identified lycopane (2,6,10,14,19,23,27,31-octamethyldotriacontane) and several pentacyclic triterpenes (molecular mass M=440, thereafter referred to as "triterpenoids") such as β-amyrin Methyl Ether (ME) (Olean-12-ene-3β-ol), Germanicol ME (Olean-18-ene-3β-ol) and Taraxerol ME (Taraxer-14-en-3β-ol) (Fig. S2).

https://doi.org/10.5194/cp-2020-114
Preprint. Discussion started: 2 October 2020

Climate of the Past Discussions
Open Access
EGU

239 The polar fraction of 61 samples, containing the glycerol dialkyl glycerol tetraethers (GDGTs), was dissolved in a
240 mixture of 99:1 (v/v) hexane/propanol and filtered through 0.45 mm PFTE filters. GDGTs were analysed (in
241 triplicate) by high performance liquid chromatography (HPLC)/MS in single ion monitoring mode on an Agilent
242 1100 series LC/MSD SL (Hopmans et al., 2004; Schouten et al., 2007).

Figure 4

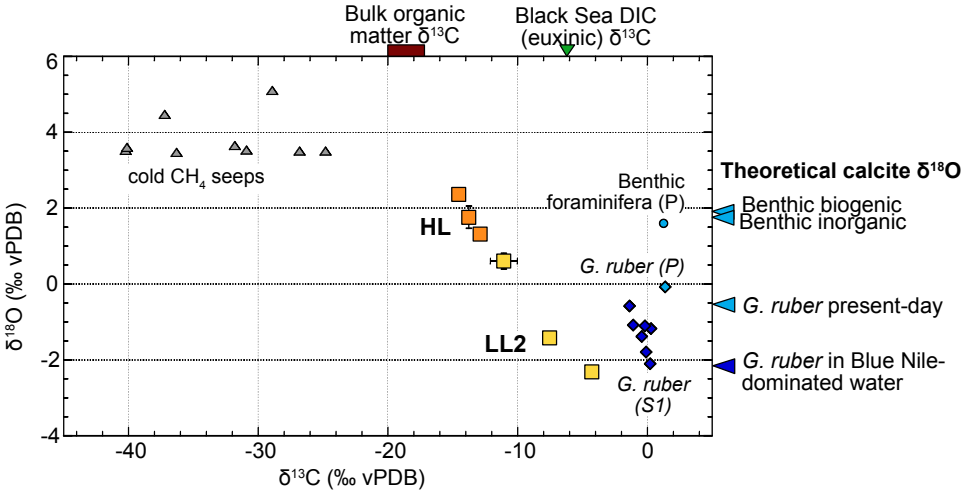

243

244 **Figure 4. Isotopic signature of the LL2 and HL sublayers. Scatter plot of $\delta^{18}O$ vs $\delta^{13}C$ values of three LL2 sublayers (yellow) and**
245 **three cemented HL (orange), as compared to isotopic signatures of methane-derived carbonates from the eastern Mediterranean**
246 **(grey triangles) (Aloisi et al., 2000; Bayon et al., 2013), top-core benthic (light blue circle) and planktonic foraminera (light blue**
247 **diamond), sapropel S1 planktonic foraminifera (dark blue diamonds) and bulk organic matter $\delta^{13}C$ (brown rectangle) from core**
248 **P33, Black Sea (euxinic) DIC $\delta^{13}C$ signature (green triangle) (Fry et al., 1991) and theoretical $\delta^{18}O$ signature of biogenic and**
249 **inorganic benthic and planktonic calcite (blue triangles) (Tab. S4).**

250

251 ## 4 Results and interpretation

252 ### 4.1 Sedimentary patterns on the western Nile deep-sea fan

253 The deeper core P33 exhibits a near-continuous 500-cm laminated interval between ca. 100 cm core depth and the
254 bottom of the core, with high Ti/Ca ratios and high sedimentation rates (between 100 and 350 cm/ka) (Fig. 2a). A
255 40-cm interruption with poorly defined laminations and traces of bioturbation occurs in the upper part of the
256 laminated interval between 140 and 100 cm core depth (Fig. 2a). The intermediate depth core P73 shows a series
257 of laminated intervals between 200 cm and the bottom of the core, which are accompanied by high Ti/Ca ratios
258 and high sedimentation rates (between 150 and 250 cm/ka) (Fig. 2b). Several interruptions with poorly-laminated

https://doi.org/10.5194/cp-2020-114
Preprint. Discussion started: 2 October 2020


Climate of the Past Discussions

to non-laminated (bioturbated) intervals are identified at 480 cm, 370 cm, 240-290 cm and 215 cm. In contrast to the two deeper cores, the shallower core P99 is generally non-laminated with the exception of faint to well-defined laminations at 510-520 cm, 490 cm, 470 cm, 405 cm, 340 cm, and 180-200 cm core depth (Fig. 2c). However, both the Ti/Ca records and sedimentation rates exhibit changes similar to the two deeper cores with higher values between 200 cm core depth and the bottom of the core (sedimentation rates of ca. 200 cm/ka).

4.2 Structure and composition of the laminations

The lamination structure is regular throughout core P33 and similar to the laminations in core P73 and P99 (Fig. S3). Well-defined laminations are composed of an alternation of dark and light bands forming sublayers, whereby dark sublayers (DL) are mostly thicker (0.2 and 15 mm) than light sublayers (0.1 to 0.4 mm) (Fig. 3). The mineral composition of DL (Fig. 3c) consists of clay minerals (kaolinite, illite and smectite) as well as silt-size detrital minerals (quartz, plagioclase, pyroxene, iron-titanium oxides). Subdivisions of DL into potassium (K)-rich (labelled DL1) and titanium (Ti)-rich (labelled DL2) parts are observed in thicker laminations. These can be distinguished by XRF elemental mapping as well as by their texture, Ti-rich sublayers containing coarser particles (ca. 20-30 µm) as K-rich sublayers (Fig. 3a, 5b).

Light sublayers (LL) contain predominantly carbonate and can be subdivided into two main types (Fig. 3a). The light-layer type 1 (LL1) are diffuse sublayers of silt-sized (ca. 10-20 µm) and unsorted particles containing biogenic carbonates (coccoliths and foraminifera) and quartz grains (Fig. 3a). Foraminifera shells generally contain small grains of iron sulphides, which may have formed on organic residues (Fig. S4). Some of these sublayers present a slight cementation. The light sublayers type 2 (LL2) contain well-sorted fine (ca. 1-10 µm) and needle-shaped calcite minerals, mixed with detrital silicate grains including clay minerals (Fig. 3). The detrital assemblage in LL2 sublayers is similar to that of dark layers but contains a larger amount of calcite (Fig.3c). LL2 sublayers are abiotic, have a wavy internal structure and contain concentrated lenses of carbonate grains (Fig. 3a). Some of these sublayers show a sharp lower boundary and either an upward decrease or increase in grain concentration (Fig. 3a). In the lower part of core P33, three prominent LL2 sublayers are cemented and consolidated (thereafter denoted "hard layers" HL) and are generally thicker than the softer LL2 sublayers (Fig. 2a). Four similar HL are also found in core P73 (Fig. 2b). The presence of organic matter is observed either within LL or at the base of DL.

https://doi.org/10.5194/cp-2020-114
Preprint. Discussion started: 2 October 2020

Climate of the Past
Discussions
Open Access
EGU

Figure 5

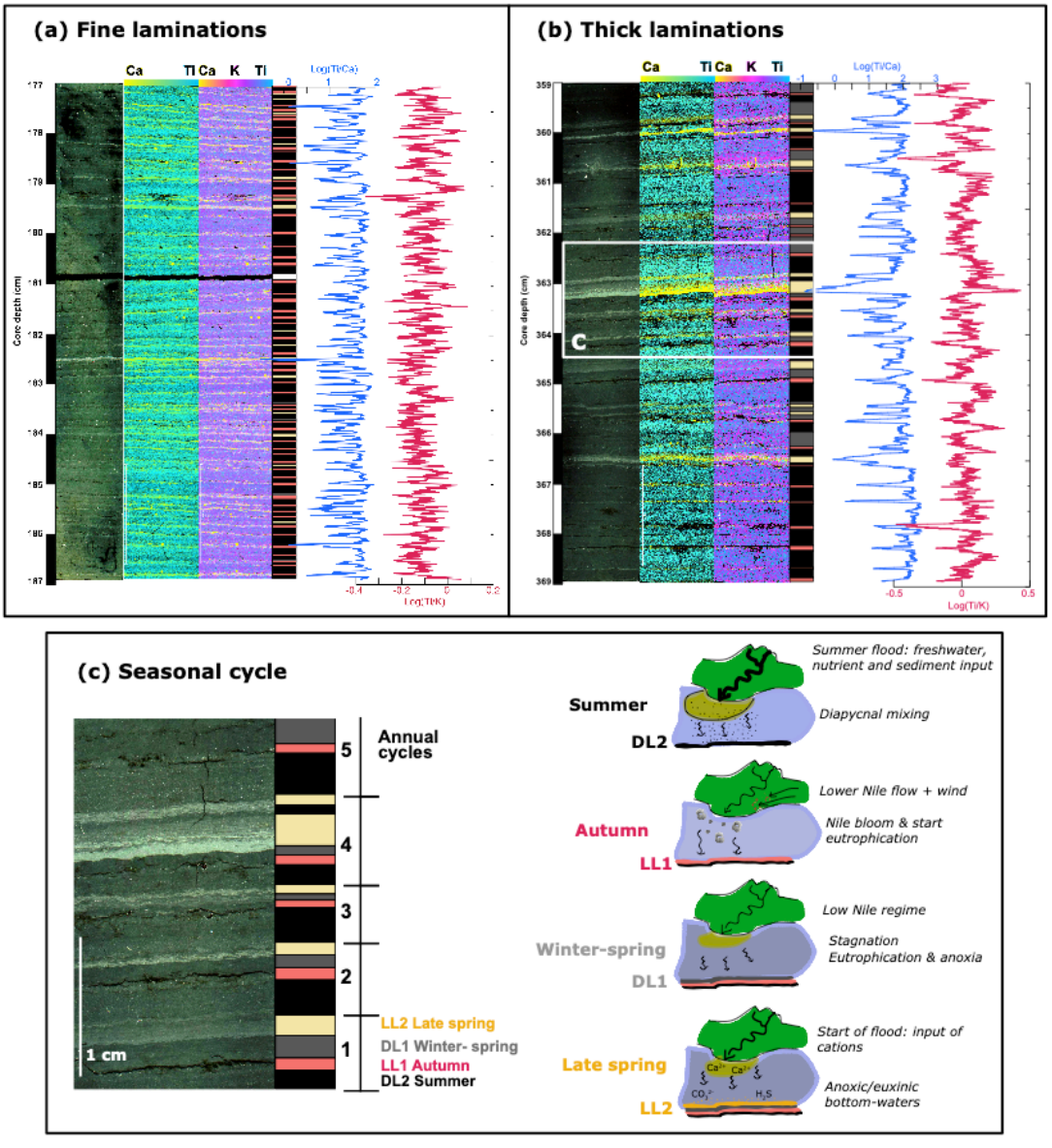

Figure 5. Laminations and seasonal cycle in core P33. (a) Fine laminations and (b) thick laminations from sections located at ca. 180 and 360 cm core depth, respectively. From left to right: core depth (cm), cross-polarized scan of the thin section, elemental mapping showing relative amounts of calcium (Ca, yellow) versus titanium (Ti, turquoise), elemental mapping showing relative amounts of calcium (Ca, yellow), potassium (K, pink) and titanium (Ti, blue), schematic lithological log with color-coded sublayer type (LL1: pink, DL1, grey, LL2: yellow and DL2: black), down-section profile of log(Ti/Ca) (blue) and log(Ti/K) (red). (c) Blow-up from the white rectangle in (b), showing the seasonal cycle as drawn by sublayer succession. From left to right: part-polarized microscope image, sublayer identification, determined season for each sublayer type and number of annual cycles in the sample. Right hand-side: sketches of an annual cycle as derived from microfacies analyses from summer (top) to late spring (bottom).

https://doi.org/10.5194/cp-2020-114
Preprint. Discussion started: 2 October 2020


Climate of the Past Discussions

Stable $\delta^{18}O$ and $\delta^{13}C$ isotope measurements were performed on a set of 6 LL2 and HL sublayers ranging in thickness from 0.1 to 0.8 mm (Fig. 4). Cemented HL have a strongly depleted $\delta^{13}C$ (-10 to -15 ‰) and an enriched $\delta^{18}O$ (0.5 to 2.5 ‰) signature compared to the softer LL2 sublayers (with $\delta^{13}C$ between -11 and -5 ‰ and $\delta^{18}O$ between 0.5 and -2 ‰). These carbonates show a wide range of stable oxygen and carbon isotope values and apparently fall on a mixing line between a depleted $\delta^{13}C$/heavy $\delta^{18}O$ and an enriched $\delta^{13}C$/light $\delta^{18}O$ end-member, which do not correspond to either biogenic carbonates or regional methanogenic carbonates (Fig. 4).

The sublayers are deposited in a remarkably constant succession over the length of the laminated interval (Fig. 5). This succession is particularly clear in the thicker laminations and follows the pattern from bottom to top: LL1, DL1, LL2 and DL2. Sublayers LL1 and DL2 are always present in the succession, whereas DL1 is sometimes very thin or not detectable and LL2 can be missing (Fig. 5b). In the lower part of the core (between 260 and 570 cm) sub-layers are on average thicker and thinner in the upper part of the laminated interval. At our core sites, we did not identify any remains of diatoms.

Anomalously thick layers (mm- to cm-scale) were identified throughout the record and labelled event layers (EL). These well-mixed layers containing matrix-supported grains and showing a clear bimodal distribution of silt- (ca. 15-20 µm) and mud-sized particles. In general, EL have sharp but non-erosive boundaries and either no clear internal structure or show a fining upward.

4.3 Spatial and temporal correlations

4.3.1 Tracers of past oxygenation conditions

In order to reconstruct past changes in oxygenation conditions, we used four independent tracers: the presence of laminations and lycopane, the benthic foraminifera assemblage and the sulphur to chlorine (S/Cl) ratio. Well-preserved laminations in the sediments implies the existence of suboxic to anoxic conditions in the bottom waters that prevented the development of foraging fauna (Schimmelmann et al., 2016). The laminated intervals coincide with high sedimentation rates (> 100 cm/ka, Fig. 2) in all cores with suboxic to anoxic conditions at all water depths between 9.5 and 7.5 ka BP and stable oxic conditions that establish between 7.0 and 6.0 ka BP (Fig. 6). The occurrence of lycopane is an additional indicator of depositional anoxic conditions given that this biomarker degrades under oxic conditions (Sinninghe Damsté et al., 2003) (Fig. 6b,g). Changes in the assemblages of benthic foraminifera (Fig. 6h) provide additional information of the oxygenation and trophic conditions of the benthic ecosystems: i) the epifaunal species *Planulina* spp. and *Cibbides* spp. are indicative of well-oxygenated conditions and oligo- to mesotrophic conditions, ii) the shallow infaunal species *Bolivina/Brizalina* spp. and *Uvigerina* spp.

https://doi.org/10.5194/cp-2020-114
Preprint. Discussion started: 2 October 2020

are tolerant to suboxic conditions and meso- to eutrophic conditions and, iii) the deep infaunal species *Globobullimina* spp. and *Chillostomella* spp. are well adapted to anoxic conditions (Abu-Zied et al., 2008; Jorissen, 1999; Schmiedl et al., 2003). Finally, the S/Cl records (Fig. 6a,d,f) trace the diagenetic formation of sulphur minerals such as pyrite (FeS_2), greigite (Fe_3S_4) or pyrrhotite (Fe_7S_8) from the pore-water sulphides (Liu et al., 2012; Matthews et al., 2017; Revel et al., 2015). This process is favoured by oxygen depletion, which leads to the accumulation of dissolved sulphides in the pore-waters and precipitation of solid iron sulphides. These iron sulphides are generally resistant to post-depositional oxygenation and therefore permit the identification of past hypoxic intervals that might have be partly reoxidized (Larrasoaña et al., 2006). All proxy-records document suboxic to anoxic conditions at all water depths between 9.5 and 7.5 ka BP and stable oxic conditions that establish between 7.0 and 6.0 ka BP (Fig. 6).

In the shallowest core P99, several short-term faintly-laminated intervals are observed between 9 and 8.3 ka BP and between 7.6 and 7.4 ±0.3 ka BP (Fig. 6c), which contain well-preserved laminations and a peak value of lycopane mass accumulation rates (MAR) (up to 0.013 µg/cm^2.a) at 7.5 ±0.3 ka BP (Fig. 6b). High S/Cl values occur between 9 and 8.5 ka BP, but are interrupted by a strong drop around 8.7 ka BP. Values decrease after 8.5 ka BP, but remain slightly elevated between 8.5 and 7.2 ka BP (Fig. 6a).

In intermediate depth core P73, laminations occur as a nearly continuous interval between 9.2 ±0.6 and 7.4 ka BP with an interruption between 8.3 and at 7.6 ka BP (Fig. 6e). High S/Cl values occur between 9.6 and 7.5 ka BP, with a strong drop in the non-laminated interval around 7.9 ka BP. The S/Cl record shows a gradual decrease between 7.3 and 6 ka BP, after which the record remained low and only varied slightly (Fig. 6d).

In the deepest core P33, laminations occur continuously between 9.6 and 8.1 ka BP, followed by an interval of faint laminations until 7.3 ka BP (Fig. 6i). Lycopane MAR follow the lamination pattern with high values in the laminated interval between 9.6 and 8.1 ka BP (between 0.1 and 0.35 µg/cm^2.a) and a gradual decrease in the faintly-laminated interval until 7.3 ka BP (from ca. 0.01 µg/cm^2.a to less than 0.001 µg/cm^2.a) (Fig. 6g). The S/Cl record shows generally higher values between 10 and 7.5 ka BP with lower values between 9.5 and 9.0 and around 8.8, 8.3, and 8 ka BP (Fig. 6f). The S/Cl record rapidly decreases between 7.5 and 6.5 ka BP and then remains at low values in the younger part of the core. The laminated interval between 9.6 and 8.1 ka BP is devoid of benthic foraminifera (except at 8.55 ka BP), after which infaunal species reappear (with a peak around 7.8 ka BP) but their presence remains very volatile until ca. 7.4 ka BP (Fig. 6h). Epifaunal species indicative of well-oxygenated and oligotrophic bottom waters are absent throughout the early Holocene record but a few specimens are observed at ca. 7.5 and 6.7 ka BP (*Cibbides* spp. and *Planulina* spp., respectively).

https://doi.org/10.5194/cp-2020-114
Preprint. Discussion started: 2 October 2020

Climate of the Past Discussions

Figure 6

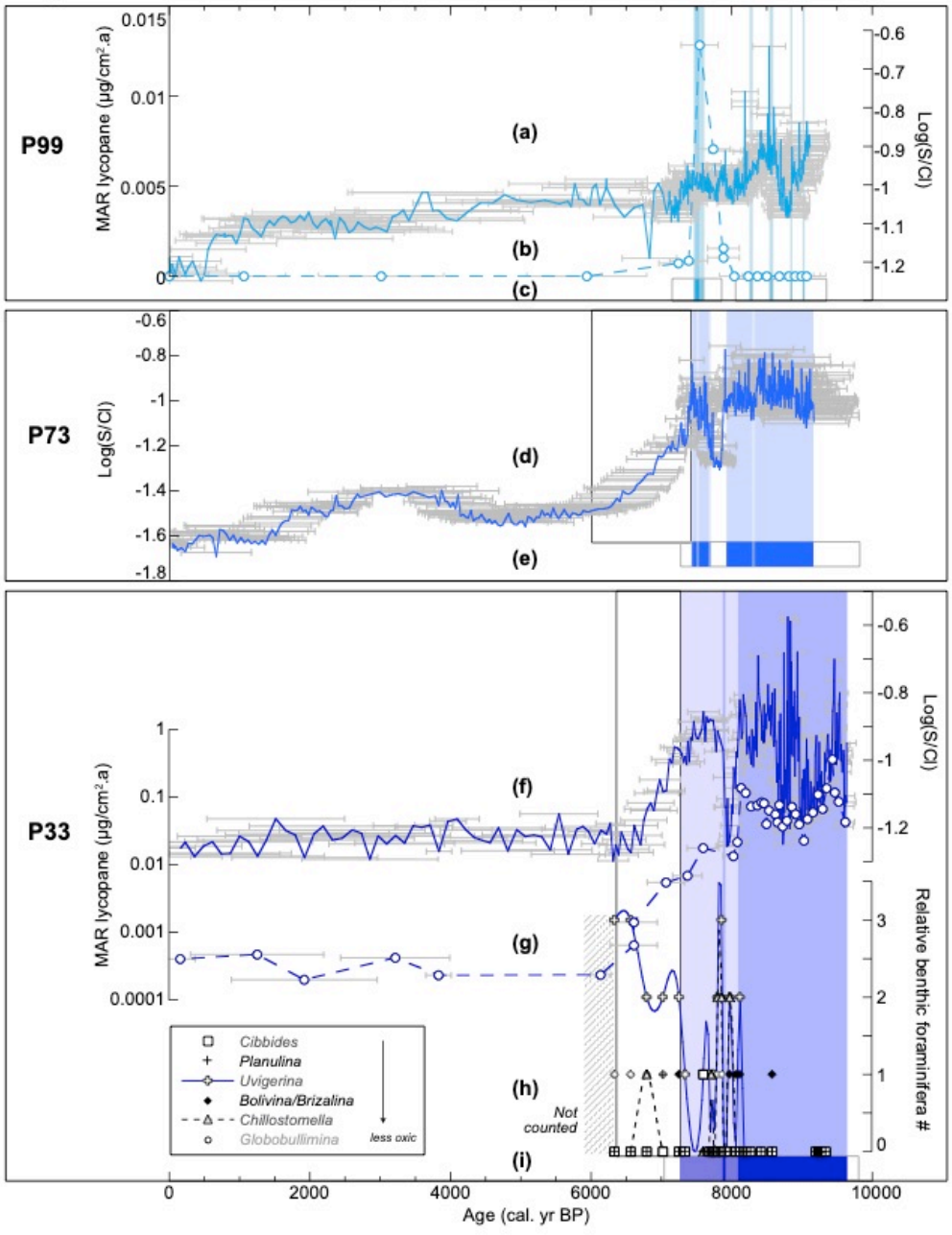

Figure 6. Proxies of paleo-oxygenation in cores P99 (turquoise, a-c), P73 (blue, d-e) and P33 (dark blue, f-i) on age scale (0-10 ka BP). (a,d,f) Log-ratio of S/Cl (continuous lines). (b,g) Mass accumulation rates (MAR) of lycopane (dashed lines and circles). Grey bars show the age uncertainty. (c,e,i) Lamination pattern (darker boxes: laminated, lighter boxes: faint laminations and grey boxes: age uncertainty). (h) Benthic foraminifera in core P33 with genus identification (see legend) and relative scale (1: <10, 2: 10-30, 3 >30 individuals counted). Trends shown by cubic splines (continuous line through *Uvigerina* counts and dashed line through *Chillostomella* counts). Open boxes in P73 and P33: interval of reoxygenation after sapropel S1 deposition.

https://doi.org/10.5194/cp-2020-114
Preprint. Discussion started: 2 October 2020


Climate of the Past Discussions

360 **4.3.2 Dynamics of primary productivity**

361 Changes in primary productivity off the Nile mouth was traced using MAR of C_{37}-alkenones and crenarchaeols in
362 cores P99 and P33 (Fig. 7). Alkenones are produced in surface waters by haptophyte algae, in particular the
363 coccolithophorid *Emiliana huxleyi* (Marlowe et al., 1984; Volkman, 2000) while the biological source of
364 crenarchaeol are thaumarcheota living throughout the water column but concentrated in the upper part of the water
365 column in the Mediterranean Sea (Besseling et al., 2019). Alkenones and crenarchaeols MAR are of similar order
366 of magnitude in both cores (up to 0.3 $\mu g.cm^{-2}.a^{-1}$ and 3.5 $\mu g.cm^{-2}.a^{-1}$, respectively). The overall patterns of changes
367 in biomarkers are similar in both cores, with highest contents being measured between 10 and 7 ka BP.
368 Several short pulses of alkenone and crenarchaeol deposition are observed in shallowest core P99 at 9.1, 8.8, 8.5,
369 8 and 7.5 ka BP (all dates ±0.25 ka BP) (Fig. 7a,b), although the alkenone MARs do not show large peaks between
370 9 and 8.5 ka BP (Fig. 7a). There is a clear correspondence between the occurrence of peaks in MAR of organic
371 compounds and the presence of faint and well-preserved laminations (Fig. 7c).
372 In deeper core P33, the sampling resolution is higher and the signal is spikier (Fig. 7d,e). The MARs of both
373 crenarchaeols and alkenones are higher in the laminated interval between 9.6 and 8.2 ka BP (±0.1 ka BP) and in
374 the faintly laminated interval between 8.2 and 6.5 ka BP (±0.1 ka BP) (Fig. 7f).
375 In nearby and deeper cores MS27PT and GeoB7702-3 (Fig. 7 g,h), crenarchaeol MARs are also higher between 10
376 and 8 ka BP, but MARs are highest between 10 and 8.5 ka BP in core MS27PT while a marked peak occurred in
377 core GeoB7702-3 at ca. 8.1 ka BP (Castañeda et al., 2010; Ménot et al., 2020).

378 **4.3.3 Dynamics of river runoff and sediment input**

379 The changes in river runoff and sediment input to the Nile DSF were reconstructed using major elemental contents,
380 MAR of branched GDGTs (brGDGTs), odd long-chain *n*-alkanes and triterpenoids, the oxygen isotopic
381 composition of foraminifera and sedimentation rates (Fig. 8). Following previous inferences (Billi and el Badri Ali,
382 2010; Blanchet et al., 2013; Garzanti et al., 2015), we use the Ti/Ca and Ti/K ratios to trace the relative variations
383 of terrigenous input and grain size (Fig. 8a,e,h). We also used the recalculated oxygen isotopic composition of the
384 seawater ($\delta^{18}O_{sw}$) as a tracer of freshwater input, with lower values reflecting a larger influence of Nile-derived
385 waters on the shelf (Blanchet et al., 2014) (Fig. 8i). Finally, runoff is estimated using MAR of biomarkers specific
386 of terrestrial organic matter, such as brGDGTs, odd long-chain *n*-alkanes and triterpenoids (Fig. 8c,k). Branched
387 GDGTs mostly derive from soil organic matter but contributions from riverine and marine (in-situ) organic matter
388 have been detected in deltaic systems (De Jonge et al., 2014; Sinninghe Damsté, 2016; Xiao et al., 2016). According

https://doi.org/10.5194/cp-2020-114
Preprint. Discussion started: 2 October 2020

Climate of the Past Discussions
Open Access
EGU

389 to their mean carbon preference index of 6.6, the odd long-chain *n*-alkanes mostly originate from terrestrial sources
390 (Blanchet et al., 2014; Bray and Evans, 1961) and triterpenoids are higher plants biomarkers (Diefendorf et al.,
391 2012; Jacob et al., 2005). The overall patterns of changes in terrigenous input are similar in all cores, with highest
392 contents being measured between 10 and 7 ka BP.
393

Figure 7

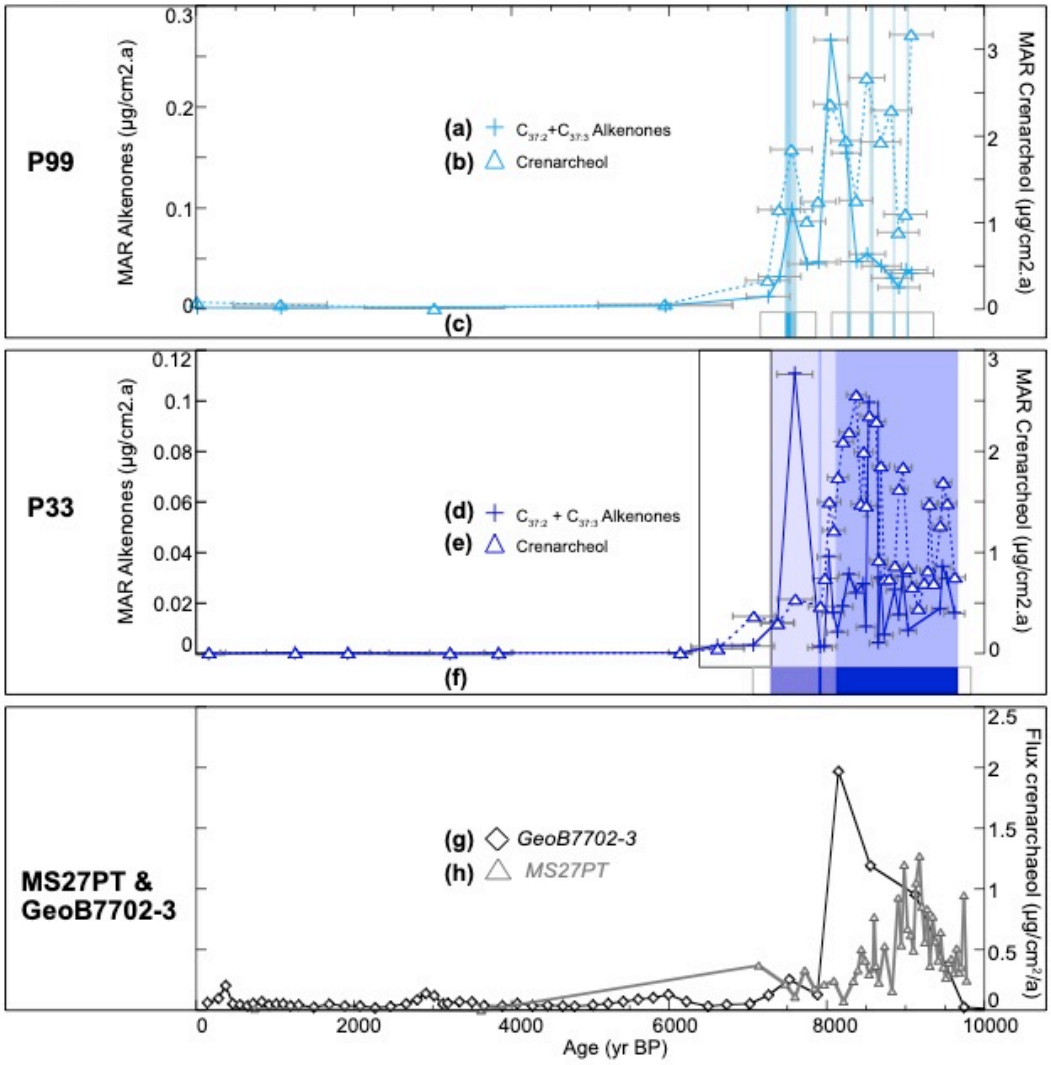

394

395 **Figure 7. Proxies of primary productivity in cores P99 (turquoise, a-c), P33 (blue, d-f), GeoB7702-3 (black, g) and MS27PT (grey, h)**
396 **on age scale (0-10 ka BP). (a,d) Mass accumulation rates (MAR) of alkenones (crosses and continuous lines). (b,e,g,h) MAR of**
397 **crenarchaeol for cores P33 and P99 (triangles and dashed lines), GeoB7702-3 (black diamonds) (Castañeda et al., 2010) and MS27PT**
398 **(grey triangles) (Ménot et al., 2020). (c,f) Lamination pattern (similar colour coding as in Fig. 5). Grey bars show the age uncertainty.**

https://doi.org/10.5194/cp-2020-114
Preprint. Discussion started: 2 October 2020


Climate of the Past Discussions

The Ti/Ca and Ti/K records of all three cores ratios show very similar patterns with relatively high amounts of Ti in the Early Holocene (ca. 10-7.5 ka BP) and the Late Holocene (1-0 ka BP) (Fig. 8a,e,h). Especially in well laminated cores P73 and P33, high-frequency fluctuations in the Ti/Ca records during the Early Holocene are related to the presence of Ca-rich laminations (Fig. 5). Although the magnitude is not similar in each core, rapid decrease in Ti/Ca records around 7.2 ka BP marks a reduction of the lithogenic input (fig. 8a,h) and is followed by a more gradual decrease until ca. 3-4 ka BP. This gradual decrease is also recorded in the $\delta^{18}O_{sw}$ (Fig. 8i). The decrease in lithogenic input at 7.2 is accompanied by a simultaneous increase of K-rich material (fig. 8a,e,h). A stepwise increase in Ti/Ca and Ti/K (and to a lesser extend in $\delta^{18}O_{sw}$) is observed in all cores between 3-3.5 and 1 ka BP.

Sedimentation rates (SR) were calculated linearly between dated points (Table 2) (Fig. 8b,f,j). They are of the same order of magnitude and vary synchronously in the three cores with highest SR during the sapropel (i.e., >100 cm/ka between ca. 10 and 7 ka BP). An abrupt decrease is recorded in cores P99 and P73 around 7 ka BP whereas SR decreased more gradually from 9 to 7 in core P33. After 7 ka, the SR remained below 20 cm/ka in all three cores.

The MAR of *n*-alkanes and triterpenoids are a factor 10 higher in core P33 than in core P99 (resp. up to 7 and 0.6 $\mu g.cm^{-2}.a^{-1}$) but brGDGTs MAR are of a similar order of magnitude in both cores (resp. up to 0.3 $\mu g.cm^{-2}.a^{-1}$ and 4 $\mu g.cm^{-2}.a^{-1}$) (Fig. 8c,k). Several pulses of terrestrial organic matter input are observed in shallowest core P99 at 9.1, 8.8, 8.5, 8.2 and 7.5 ka BP (all dates ±0.25 ka BP) (Fig. 8c). There is a good agreement between the occurrence of peaks in MAR of organic compounds and the presence of faint versus well-preserved laminations (Fig. 8d). In deeper core P33, the MAR are higher in the laminated interval between 9.6 and 8.2 ka BP (±0.1 ka BP) but both brGDGT and high plant *n*-alkanes and triterpenoids show low MARs in the faintly laminated interval between 8.2 and 6.5 ka BP (±0.1 ka BP) (Fig. 8k,l).

5 Discussion

5.1 Seasonal dynamics over the Nile deep-sea fan as derived from microfacies analyses

As shown by the microfacies analyses, the total layer thickness is mainly controlled by terrigenous inputs (DL) (Fig. 5). The calcium carbonate-rich layers (LL) only represent a minor contribution in terms of sediment budget. As shown in Fig. 5b, the sequence of dark and light sublayers (DL2, LL1, DL1, LL2) is consistent throughout the laminated interval, even though sub-layers DL1 and LL2 can be very thin and sometimes absent. We propose that the different sublayers recorded distinct depositional regimes throughout the year and represent an annual cycle.

https://doi.org/10.5194/cp-2020-114
Preprint. Discussion started: 2 October 2020

Climate of the Past Discussions
Open Access
EGU

Figure 8

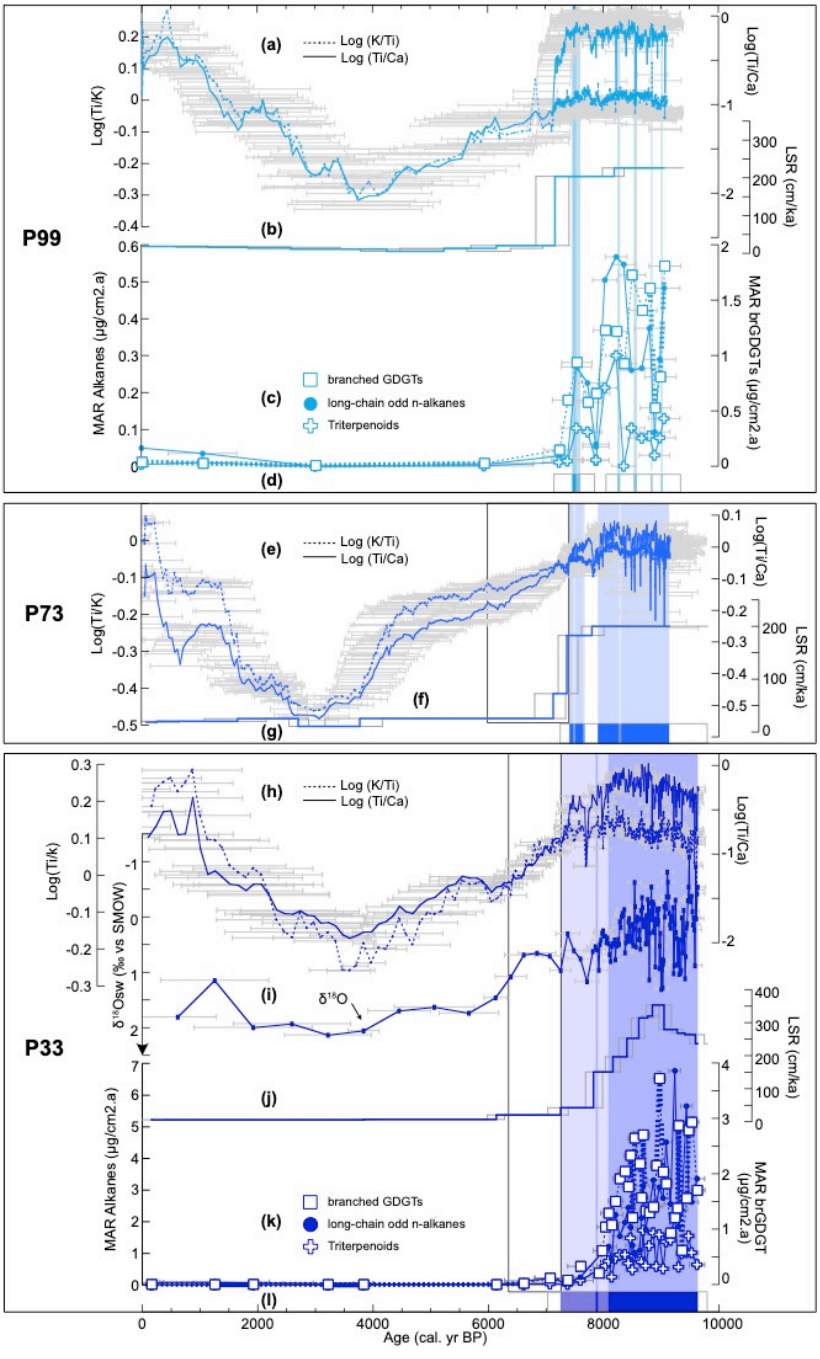

Figure 8. Proxies of terrigenous input in cores P99 (turquoise, a-d), P73 (blue, e-g) and P33 (dark blue, i-m) on age scale (0-10 ka BP). (a,e,i) Log(Ti/Ca) (continuous lines) and Ti/K (dashed lines). (b,f,k) sedimentation rates. (c,k) Mass accumulation rates (MAR) of odd long-chain *n*-alkanes (circles and continuous lines), triterpenoids (crosses and continuous lines) and branched GDGTs (squares and dashed lines). (d,g,l) Lamination pattern (similar colour coding as in Fig. 5). (i) Calculated $\delta^{18}O$ surface seawater for core P33 (reversed y-scale) (Blanchet et al., 2014). Grey bars show the age uncertainty.

https://doi.org/10.5194/cp-2020-114
Preprint. Discussion started: 2 October 2020


Climate of the Past Discussions

The coarser grained (ca. 20-30 µm) DL2 sublayer is proposed to represent sediments deposited during summer floods of the Nile River. The present particulate matter transported during peak Nile discharge is indeed marked by a silt to fine sands grain-size (Billi and el Badri Ali, 2010). Mineralogical analyses of the DL2 sublayers shows the presence of smectite, plagioclases and iron-titanium oxides, which are typical erosion products of basaltic rocks of the Ethiopian volcanic plateau (Garzanti et al., 2015, 2018) (Fig. 3c). In the marine environment, low-density fresh-water flood plumes of Nile summer floods have been associated with the formation of hyperpycnal plumes, which distribute coarser-grained sediments through formation of downward-flowing sediment-laden fingers (Ducassou et al., 2008; Parsons et al., 2001). The thick DL2 layers observed throughout the record match the depositional expression of hyperpycnal plumes and associated Nile summer floods. In addition to this regular pattern, exceptional flood events have been identified in several sediment archives over the western deep-sea fan based on the occurrence of mud clasts, and correspond in our record to the thick EL (Mologni et al., in press).

The detrital DL2 sublayers are overlain by coarse-grained light sublayers (LL1) that are enriched in biogenic carbonates, mostly foraminifera and coccoliths (Fig. S4). This biogenic carbonates assemblage resemble that of the so-called “Nile blooms”, which occurred in September-October prior to the construction of the Aswan Dam in 1965 (Nixon, 2003). Fertilisation of the surface waters off the Rosetta mouth by large nutrients input during the summer Nile floods triggered an algal bloom, upon which zooplankton grazed. This was marked by the production of carbonate organisms such as coccoliths and foraminifera, like in LL1 sublayers (Halim et al., 1967). Occasional, these layers contain quartz grains that might be related to autumn-early winter dust storms (Goudie and Middleton, 2001).

The following sublayer DL 1 is generally a fine-grained homogenous dark layer, which is enriched in potassium and reflects winter and spring deposition. Analysis of the present suspension load of the Nile River shows that the suspended load of the main Nile is enriched in clay particles during low Nile discharge periods (i.e., from late autumn to early summer) (Billi and el Badri Ali, 2010; Garzanti et al., 2006).

Sublayers DL1 are often overlain by a final sublayer of homogenous fine calcite grains (LL2) that is sometimes cemented (HL). The internal draping structure of these layers suggests that these calcite grains formed close to the seafloor, either in seawater or in highly porous sediments at the water-sediment interface. The mineralogical assemblage in these layers is similar to the detrital-rich layers but shows an enrichment in calcite (Fig. 3c). SEM pictures suggest that microcrystalline calcite might have formed as a coating on the detrital grains, which could have served as nucleus (Fig. 3b). Signs of sedimentary disturbance associated with diagenetic carbonate formation during sediment compaction are only observed in the cemented layers. Furthermore, these LL2 sublayers are also identified both in cores P73 and P99 with sublayer structures similar to those of core P33 (Fig. S3). This points to

https://doi.org/10.5194/cp-2020-114
Preprint. Discussion started: 2 October 2020


Climate of the Past Discussions

a regionally ubiquitous formation of authigenic carbonates in the water column, whereas post-depositional diagenetic processes are more pervasive and local. These layers are linked to the late spring-early summer season and the potential formation pathways and implications for seawater chemistry will be discussed in section 5.2.

5.2 Seasonal changes in physical and chemical properties of seawater

The seasonal sequence of sublayers depicted above for core P33 provides new insights into the variability of chemical and physical parameters of seawater offshore the Nile mouth. The DL2 sublayers were deposited during the summer floods of the Nile River. According to present-day and historical observations (Halim et al., 1967), summer floods lead to the formation of a freshwater plume above an underlying highly saline seawater mass (Fig. 1a). During sapropel S1, this low-salinity subsurface water mass extended much further offshore in the whole eastern Mediterranean basin, as shown by species-specific oxygen isotopes of planktonic foraminifera deposited south of Crete (Tang and Stott, 1993). The large input of freshwater is thought to have led to a strong density-driven stratification of water masses in the eastern Mediterranean (Kemp et al., 1999). However, the important sediment loading of Nile-derived freshwater that entered the relatively saline eastern Mediterranean probably played an important role in driving the mixing of fresh- and seawater, through double-diffusive mixing and the formation of salt fingers (Parsons et al., 2001). In addition, these processes are also thought to drive nutrient exchange across stratified water-masses (Oschlies et al., 2003). The release of nutrients and their exchange across waters masses during summer floods fuelled primary productivity in the whole eastern Mediterranean (Mojtahid et al., 2015) and triggered "Nile blooms" in autumn, clearly evidenced in our record by zooplankton shells in LL1 sublayers. High levels of primary productivity probably triggered a gradual eutrophication of the underlying water masses due to bacterial oxidation of sinking organic matter. The deposition of fine-grained clay-rich particles following these "Nile blooms" occurred during the late autumn to early summer low discharge regime of the Nile River (DL1 layers). The ability to deposit clay-sized particles as laminated layers suggests a hydrodynamically stagnant water mass, which might have reinforced the gradual eutrophication of deeper water masses.

The occurrence of bottom water-derived authigenic calcite sublayers (LL2) in core P33 provides a unique opportunity to investigate seawater chemistry using their oxygen and carbon isotope signatures (Fig. 4). The $\delta^{13}C$ signatures of soft LL2 calcite sublayers suggest that they formed in euxinic (sulfidic) bottom waters dominated by respiratory processes (i.e., degradation of organic matter) similar to the present-day Black Sea (Fry et al., 1991; Nägler et al., 2011). LL2 $\delta^{13}C$ values range from -11 to -5 ‰, which is comprised between the $\delta^{13}C$ of bulk organic matter in core P33 (-17 to -20 ‰) and bottom water DIC in the euxinic Black Sea (-6.3 ‰, Fry et al., 1991) (Fig.

https://doi.org/10.5194/cp-2020-114
Preprint. Discussion started: 2 October 2020


Climate of the Past Discussions

494 4). The bathymetric $\delta^{13}C$ gradients from surface to bottom waters in core P33 is also similar to that of the present-
495 day Black Sea. The $\delta^{13}C$ ranges from 0 ‰ at the surface (as indicated by *G. ruber* $\delta^{13}C$, Fig. 4) to ca. -7‰ in
496 bottom waters offshore the Nile mouth, and from 0.8 in surface to -6.3 ‰ in bottom waters in the Black Sea (Fry
497 et al., 1991). The $\delta^{13}C$ of HL is too depleted to result from anaerobic oxidation of organic matter only and suggests
498 that part of the bottom-water DIC might have incorporated methane diffusing upwards from the sediments to
499 bottom waters. This implies a shoaling of the sulphate-methane transition zone in the water column, which has
500 been identified in the deeper parts of the Black Sea basin (Michaelis et al., 2002; Riedinger et al., 2010; Schouten
501 et al., 2001). The persistence of methane in bottom waters of the eastern Mediterranean during sapropel S1 has also
502 been proposed to account for the widespread formation of Mg-rich calcite crusts around methane seeps and vents
503 on the Nile deep-sea fan (Aloisi et al., 2002; Bayon et al., 2013). Anoxic and alkaline bottom waters at that time
504 likely prevented the oxidation of methane into CO_2 and led to the precipitation of carbonate crusts with a very
505 depleted $\delta^{13}C$ signature (-25 to -45 ‰), typical of hydrocarbon sources and clearly distinct from that of authigenic
506 carbonate layers found in core P33 (Fig. 4). However, the incorporation of methane generated at the sulphate-
507 methane transition zone from fermentation of sedimentary organic matter would provide a likely source of depleted
508 DIC to account for the low $\delta^{13}C$ of HL. It is therefore possible that methane-rich conditions developed temporarily
509 in bottom waters and led to the formation of the HL sublayers found in cores P33 and P73 (Fig. 2) as well as of
510 carbonates around cold seeps on the Nile deep-sea fan.
511 The $\delta^{18}O$ of HL sublayers is close to the theoretical $\delta^{18}O$ of inorganic carbonates formed in bottom waters (ca. 2
512 ‰) while the $\delta^{18}O$ of LL2 sublayers is similar to the theoretical $\delta^{18}O$ signature of surface waters (ca. -1 to -2 ‰,
513 Fig. 4). This indicates that temperature and salinity gradients were homogenous throughout the water column
514 during the formation of LL2 sublayers. The lowest $\delta^{18}O$ values of LL2 are similar to those of *G. ruber* formed in
515 Blue Nile-dominated/low-salinity water, which suggests that the formation of calcite in LL2 layers is related to the
516 flood season. This also supports the hypothesis of an efficient diapycnal mixing during summer floods discussed
517 earlier (Parsons et al., 2001). A potential mechanism could be the rising inflow of freshwater at the end of the
518 spring/beginning of the summer, providing cations to the sulphate-depleted and bicarbonate-rich waters that
519 developed as a result of anaerobic oxidation of organic matter off the Nile mouth (as derived from $\delta^{13}C$ signature
520 of LL2). At the end of the dry (winter) period, the Nile River water is indeed enriched in cations (Ca^{2+}, Mg^{2+})
521 (Dekov et al., 1997). In absence of additional evidence, we therefore propose that the onset of the summer flood
522 constituted a potential trigger to precipitate calcite by supplying cations to stagnating, anoxic to euxinic alkaline

https://doi.org/10.5194/cp-2020-114
Preprint. Discussion started: 2 October 2020

waters. The existence of euxinic water masses was suggested for sapropel layer S5 (Benkovitz et al., 2020; Rohling et al., 2006; Rush et al., 2019). During sapropel S1 deposition, the water column was found to be anoxic but not euxinic in the eastern Levantine basin, although strong differences in local oxygenation and chemical conditions were detected between sites (Matthews et al., 2017). It is also considered that more dysoxic conditions probably developed closer to the Nile mouth due to enhanced eutrophication (Matthews et al., 2017; Schmiedl et al., 2010; Zirks et al., 2019). These pilot isotopic results provide a first insight into deep water mass dynamics at a time when the lack of benthic foraminifera prevents the acquisition of comparable paleoceanographic information (Schmiedl et al., 2010). Analyses similar to those performed on nearby core MD9509 (isotopic signatures of molybdenum and iron) would provide valuable additional information and help to determine if bottom waters were indeed anoxic and/or euxinic (Matthews et al., 2017).

5.3 Spatial and temporal variability of deoxygenation in the eastern Mediterranean during sapropel S1

Based on the observations of seasonal sublayer deposits and in particular the occurrence of authigenic calcite, we derived that bottom waters offshore the Nile mouth were anoxic almost all-year round during sapropel S1 deposition and potentially reached euxinic and methane-rich states in spring. As similar sublayers of authigenic calcite were found in laminated intervals of cores located at shallower depths (P73 and P99, Fig. S3), we propose that similar chemical conditions occurred intermittently at depths ranging between 400 and 700 m on the western Nile deep-sea fan.

By comparing available markers of deoxygenation in the three sediment cores (in particular the S/Cl records and occurrence of laminations), we can draw a picture of changes in seawater chemistry at centennial- to millennial-scale along a bathymetric transect (Fig. 9d). We have added two deeper cores MD04-2726 and MS27PT (retrieved at 1060 and 1390 m w-d, resp.) for which S/Cl ratios were published previously (Ménot et al., 2020; Revel et al., 2015). This allows exploring changes in oxygenation state along a bathymetric transect within a newly-defined water mass located between 500 and 1800 m w-d in the Eastern Mediterranean during sapropel S1 deposition, labelled Sapropel Intermediate Water (SIW) (Zirks et al., 2019). In order to determine potential forcing factors, this bathymetric and temporal record of paleo-oxygenation will be compared with regional reconstructions of terrigenous input and primary productivity (Fig. 9a,b). As seen by microfacies analyses (section 5.1, Fig. 3), calcium mainly occurs in the marine biogenic and authigenic carbonate component (coccolithophores, foraminifera and authigenic calcite layers), whereas K and Ti occur in respectively finer- and coarser-grained detrital layers (Fig. 3).

https://doi.org/10.5194/cp-2020-114
Preprint. Discussion started: 2 October 2020

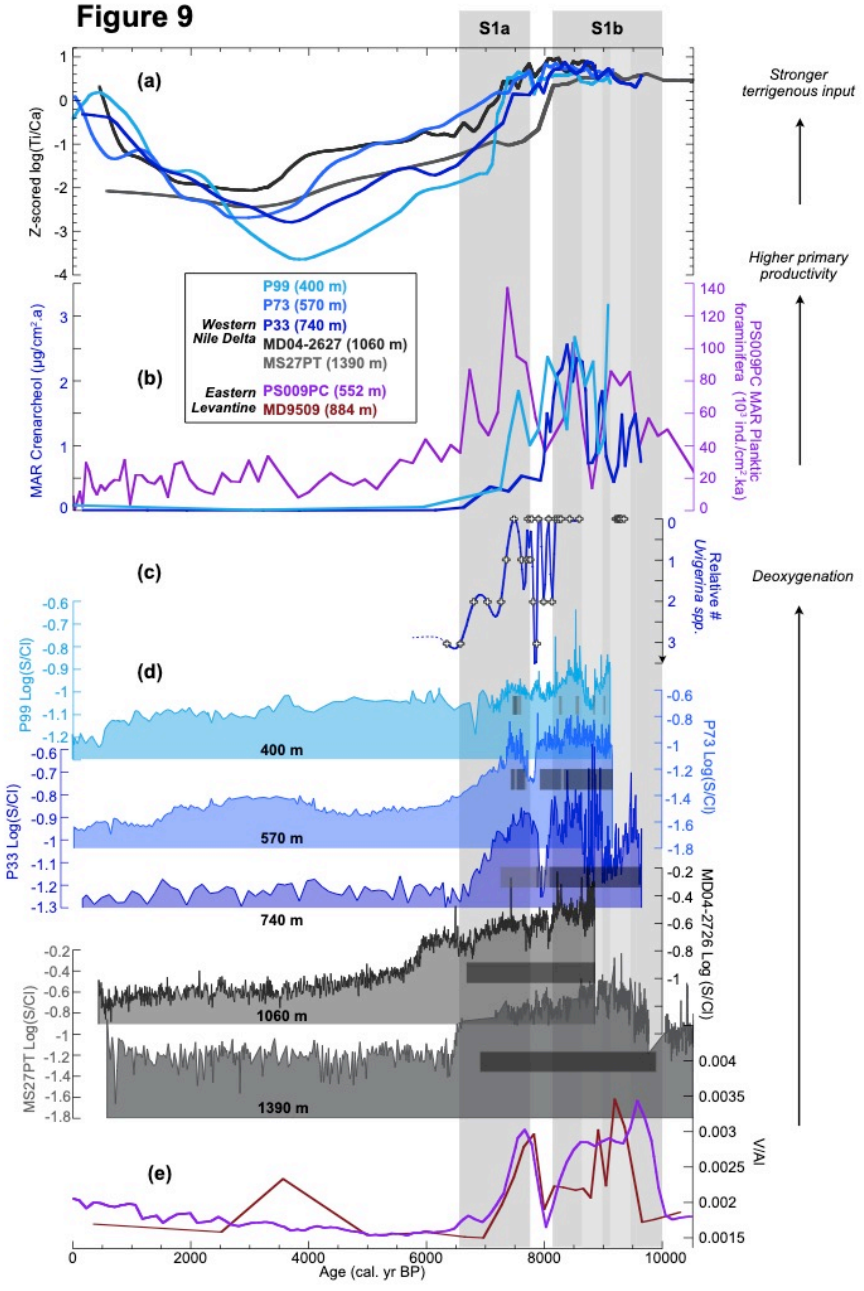

552

553 **Figure 9. Regional compilation of changes in terrigenous, primary productivity and oxygenation conditions during the Holocene. (a)**
554 **Z-scored records of log (Ti/Ca) (weighted average) of cores P99, P73, P33, MS27PT, MD04-2726 (Revel et al., 2015). Z-scoring (x-**
555 **mean(Ex)/stdev) allows to compare trends in a similar proxy from different archives by scaling the y-range and aligning the means**
556 **on 0. (b) MAR of crenarchaeol in cores P99 and P33, planktonic foraminifera in core PS009PC (Mojtahid et al., 2015). (c) Relative**
557 **abundance of benthic foraminifera *Uvigerina spp.* in core P33 (cubic spline, blue line, inverse y-scale). (d) Log(S/Cl) records and**
558 **lamination patterns in cores from the Nile DSF (shallower to deeper core site from top to bottom): P99, P73, P33, MD04-2627,**
559 **MS27PT (Revel et al., 2015). (e) V/Al records in cores PS009PC (Hennekam et al., 2014) and MD9509 (Matthews et al., 2017). Grey**
560 **vertical bars: sapropel S1a and S1b; lighter grey bars: periods of slight reoxygenation; white bar: S1 interruption (at ca. 8 ka BP).**

https://doi.org/10.5194/cp-2020-114
Preprint. Discussion started: 2 October 2020

Titanium reflects the erosion of volcanic rocks in the Blue Nile watershed (Blanchet et al., 2013; Garzanti et al., 2015), while potassium is enriched in clay minerals such as smectite and is related to low-energy Nile runoff (Billi and El Badri 2010). Therefore, we confirm the interpretation the Ti/Ca and Ti/K records as tracers of relative variations of terrigenous input and grain size (Blanchet et al., 2013) (Fig. 8a,e,i). The dynamics of terrigenous input and primary productivity are coherent over the western Nile DSF as shown by the good alignment of Ti/Ca ratios measured in all cores (Fig. 9a) and the crenarchaeol fluxes from P33, P99, MS27PT (Ménot et al., 2020; Revel et al., 2015) and GeoB7702-3 (Castañeda et al., 2010) (Fig. 7, 9b). Biomarker records can be affected by post-depositional oxidation, especially by the downward diffusion of oxygen into the reduced sapropelic sediments (i.e., a so-called burn-down process, Rutten and de Lange, 2003). However, comparable trends between biomarker records and other markers of primary productivity from regional archives that are not affected by burn-down processes (i.e., flux of planktonic foraminifera in core PS009PC, Mojtahid et al., 2015) suggest that productivity played a larger role than post-depositional oxidation in modulating the biomarker fluxes in our records (Fig. 9b).

Waxing and waning of a hypoxic water-mass during the Holocene

Prior to 10 ka BP, most sediment records from the eastern Mediterranean recorded the existence of oxic conditions as reflected by the presence of epibenthic foraminifera at water depths ranging from 500 to 2000 m (Cornuault et al., 2018; Le Houedec et al., 2020; Schmiedl et al., 2010) as well as low sulphur contents and redox sensitive element ratios (RSER) (Azrieli-Tal et al., 2014; Hennekam et al., 2014; Matthews et al., 2017; Tachikawa et al., 2015). At deep site MS27PT offshore the Nile River mouth, suboxic conditions occurred between 12 and 10 ka BP and were accompanied by higher primary productivity (Ménot et al., 2020). Such conditions have not been observed at more distal sites along the coast of Israel where primary productivity was low (Castañeda et al., 2010; Mojtahid et al., 2015).

All cores from the western NDSF show a pronounced decrease in oxygenation between 10 and 6.5 ka BP, marked by higher S/Cl records and the absence of benthic foraminifera, followed by relatively stable and oxic conditions in the younger sections of the cores (Fig. 9d). Anoxic (but not euxinic) conditions are also found at more distal locations along the path of the Levantine Jet as indicated by high vanadium to aluminium (V/Al) ratios between 10 and 7 ka BP in cores PS009PC and 9509 (located at 552 and 884 m water depth, resp.; Fig. 9e) (Hennekam et al., 2014; Matthews et al., 2017). At the scale of the Levantine basin, suboxic to anoxic conditions developed during deposition of sapropel S1 at depths ranging from 500 to >3000 m and euxinic conditions in water-depths >2000 m (ODP site 967D, Azrieli-Tal et al., 2014) and potentially in cores P33 and P73 offshore the Nile mouth (Fig. 10). There are inconsistencies as to whether the onset of anoxia occurred synchronously at all depths (Schmiedl et al.,

https://doi.org/10.5194/cp-2020-114
Preprint. Discussion started: 2 October 2020

592 2010) or spread from shallower to deeper depths between 10 and 9 ka BP (Zirks et al., 2019), which may at least
593 partly be explainable by dating uncertainties.
594 A complete reoxygenation is achieved at all depths by 6.5 ka BP (and by 6 ka at 1060 m water depth, Revel et al.,
595 2015). At the scale of the eastern Mediterranean, the recovery of benthic ecosystems appears to have followed a
596 time-transgressive pattern, with shallower sites depicting oxic conditions as early as 8 ka BP (Schmiedl et al.,
597 2010). Such a pattern is also evidenced on the western NDSF with deoxygenation conditions being maintained
598 until ca. 6.5-6 ka BP at depths >1000 m while shallower sites already started recovering around 7.5 ka BP (Fig.
599 9d).
600
601 ***Dynamic fluctuations in time and space***
602 Depth-transgressive anoxic conditions were observed repeatedly on the western Nile DSF between 570 and 1400
603 m w-d during sapropel 1a (10-8 ka BP), as indicated by the occurrence of laminations in all cores (Fig. 9d). Multiple
604 intervals of faint laminations occur in core P99 every 200-300 yrs (i.e., at 9, 8.8, 8.6, 8.3 ka BP), suggesting a
605 dynamic vertical structure of the upper boundary of the hypoxic water-mass on centennial time scales. In particular,
606 a pronounced shoaling to 400 m w-d is observed around 8.5 ka (Fig. 9d). Intermediate depth cores also show
607 variations in the oxygenation state with lower S/Cl records around 9.2 and 8.3 ka BP recorded in both cores P33
608 and P73 (although more prominent in P33) and at 8.7 ka BP recorded in core P33 (Fig. 6 and 9c). Millennial-scale
609 variations in bottom-water oxygenation were also recorded at similar depths by nearby cores PS009PC and 9509
610 as evidenced by fluctuations in the RSER (Fig. 9e) and in the benthic fauna (Hennekam et al., 2014; Le Houedec
611 et al., 2020; Matthews et al., 2017). Below 1000 m water depth on the western Nile DSF, anoxic conditions have
612 likely been more stable during S1a, as suggested by continuously laminated sapropels and relatively constant S/Cl
613 records in deeper cores MD04-2726 and MS27PT (Fig. 6, 9d). Due to complex diagenetic processes involving
614 sulphur cycling, the S/Cl may not have recorded rapid changes in the oxygenation state as shown by RSER
615 (Matthews et al., 2017; Tachikawa et al., 2015). However, the presence of continuous laminations throughout the
616 sapropel sequence strongly suggests stable anoxic conditions at depths >1000 m. An anoxic water-mass was present
617 between 500 and 3000 m w.-d. in the eastern Mediterranean during S1a, although two sites around Eratosthenes
618 Seamounts showed larger variations in oxygenation state between suboxic conditions at ca. 900 m water depth and
619 euxinic conditions at ca. 2550 m water depth (Fig. 10).
620

https://doi.org/10.5194/cp-2020-114
Preprint. Discussion started: 2 October 2020

Climate of the Past Discussions
Open Access
EGU

Figure 10

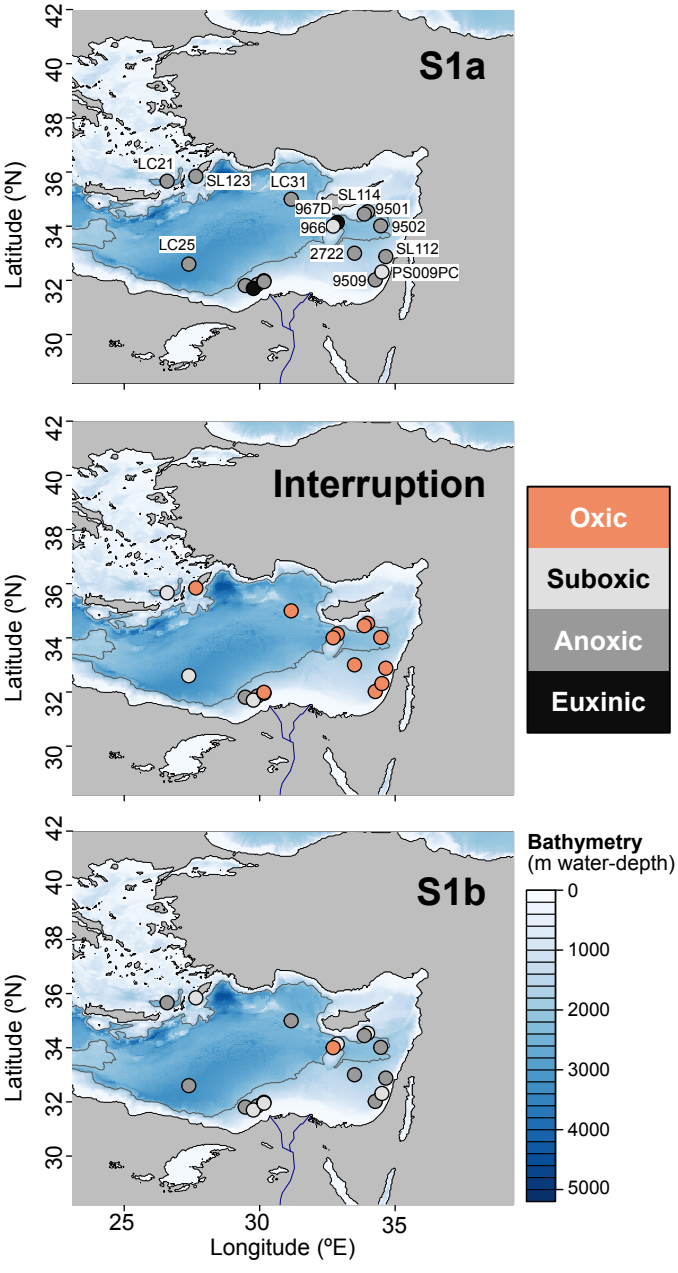

621

622 **Figure 10. Maps of deoxygenation conditions in the Eastern Mediterranean during different intervals of sapropel S1: S1a, S1**
623 **interruption and S1b. Oxygenation conditions: oxic (orange), suboxic (light grey), anoxic (grey) and euxinic (sulfidic, dark grey) in**
624 **archives located at various water depths between 400 and 3000 m (bathymetric scale at the right of the map for S1b). The dark grey**
625 **contour indicates the water-depth 1800m, which is considered the lowest bathymetric extend of the SIW (Zirks et al., 2019).**

https://doi.org/10.5194/cp-2020-114
Preprint. Discussion started: 2 October 2020

626 A pronounced but short-lasting interval of reoxidation at ca. 8 ka BP is observed on the western Nile DSF in the
627 upper 740 m, marked by a lack of laminations at 400 and 570 m depth, faint laminations and recolonization of the
628 seafloor by suboxic-tolerant benthic foraminifera at 740 m water depth and reduced S/Cl records at all depths (Fig.
629 7, 9d). The presence of continuous laminations in the deeper cores indicates that conditions remained anoxic during
630 this time interval at depths >1000 m. The reoxygenation event at 8 ka BP is a widespread marker in the eastern
631 Mediterranean generally referred to as sapropel S1 interruption, which has been related to a drastic decrease in Nile
632 runoff around the 8.2 ka event (Blanchet et al., 2013; Rohling et al., 2015). In nearby cores located above 900 m
633 water depth at the cost of Israel, the timing of this reoxygenation event was similar (Fig. 9e) (Hennekam et al.,
634 2014; Matthews et al., 2017) but these more distal cores reached a fully oxic state as indicated by the presence of
635 epibenthic fauna (Le Houedec et al., 2020; Schmiedl et al., 2010). When compiling oxygenation markers in several
636 cores from the eastern Mediterranean (Fig. 10), most sites depict a full reoxygenation from depths ranging from
637 500 to 2550 m (only two sites continue to show suboxic conditions). Low values of bottom-water $\delta^{13}C$ during the
638 S1 interruption, however, indicates stagnant water masses (Schmiedl et al., 2010). It was recently proposed that
639 this interruption is a specific feature of the so-called Sapropel Intermediate Water (SIW) mass located between 500
640 and 1800 m w.-d., within which changes in the oxygenation state may have occurred for a few hundred years (Zirks
641 et al., 2019).
642 Hypoxic conditions developed again on the western NDSF around 7.8-7.5 ka BP (sapropel S1b) (Fig. 9d). If bottom
643 waters were suboxic at 740 m as indicated by the presence of a few benthic foraminifera and faint laminations in
644 core P33, laminated intervals and high lycopene contents in cores P73 and P99 suggest that anoxic conditions
645 existed intermittently between 600 and 400 m water depth during S1b (Fig. 6a,b, 9d). At deeper sites, conditions
646 remained anoxic until ca. 6.7 ka BP when laminations stopped in core MS27PT (Fig. 9d). This suggests the
647 existence of split anoxia, during which both shallower and deeper water masses were deprived of oxygen due to
648 the respiration of rapidly-sinking organic detritus, while intermediate water masses remained suboxic (Bianchi et
649 al., 2006; Rush et al., 2019). In most cores from the eastern Mediterranean, suboxic to anoxic conditions were re-
650 established by 7.8 ka BP but generally lasted only a few hundred years and were rather unstable (Fig. 9e) (Le
651 Houedec et al., 2020; Schmiedl et al., 2010) (Fig. 10).
652
653 ***The role of runoff-driven eutrophication***
654 Recent modelling experiments indicated that the formation of a basin-wide oxygen depletion in the Mediterranean
655 Sea during sapropel S1 required a multi-millennial deep-water stagnation (Grimm et al., 2015). It was recently
656 determined that the increasing sea-level during the deglaciation allowed the inflow of fresher Atlantic-derived

https://doi.org/10.5194/cp-2020-114
Preprint. Discussion started: 2 October 2020


Climate of the Past Discussions

water, thereby decreasing the buoyancy of surface waters and deep-water ventilation in the eastern Mediterranean (Cornuault et al., 2018). This initial stagnation may have been reinforced by larger inputs of freshwater from the Nile river, which enhanced water-column stratification from 14 ka BP onwards (Castañeda et al., 2016; Cornuault et al., 2018).

The marked onset of anoxia in the eastern Mediterranean at ca. 10 ka BP is striking as it is recorded uniformly at various depths in the basin (De Lange et al., 2008; Schmiedl et al., 2010; Zirks et al., 2019). This suggests that benthic ecosystems passed a threshold that led to the development of anoxic conditions. Detailed faunal and isotopic studies showed that deep-water stagnation gradually developed from 17 ka BP onwards and that a distinct drop in $\delta^{13}C$ occurred around 11 ka BP, just before the collapse of benthic ecosystems (Cornuault et al., 2018; Schmiedl et al., 2010). It was suggested that conditions remained oligotrophic until 10 ka BP, which allowed benthic fauna to dwell even in stagnating water masses (Abu-Zied et al., 2008; Kuhnt et al., 2008). The transition to mesotrophic/eutrophic conditions occurred around 10 ka BP (Abu-Zied et al., 2008), when precipitation and runoff in the Nile River basin peaked (Castañeda et al., 2016; Weldeab et al., 2014). From 10 ka BP onwards, a drastic increase in primary productivity has been identified in the eastern Levantine Basin (Fig. 9b) (Mojtahid et al., 2015), which suggests fertilisation of surface waters by Nile-derived nutrients. It is therefore postulated that the large nutrient loading delivered by summer floods of the Nile River led to a switch from an oligotrophic to a meso- or eutrophic state in the eastern Mediterranean, which was accompanied by high levels of primary productivity in surface waters. As an extended version of the "Nile blooms" forming offshore the Nile mouth during historical times (Halim et al., 1967), peak Nile runoff during the mega-summer monsoon of the African Humid Period AHP probably fertilised large parts of the Levantine Basin during sapropel S1 deposition (Hennekam et al., 2015; Schmiedl et al., 2010). Lower oxygenation indices in cores located closer to the Nile River as shown in our study (Fig. 10) further support the pivotal impact of Nile River-induced eutrophication on the rapid spread of hypoxia in the eastern Mediterranean (Schmiedl et al., 2010; Zirks et al., 2019). Moreover, it was recently proposed that rapid changes in oxygenation could occur within 200-500 years for water masses located between 500 and 1800 m water depth due to oxygen utilization by bacterial organic matter degradation (Zirks et al., 2019). We therefore propose that most of the changes in the strength and extent of hypoxia offshore the Nile River were related to runoff-induced fertilisation and subsequent eutrophication of the water-column. However, these centennial- to millennial-scale variations were superimposed on the multi-millennial development of deep-water stagnation and suggest complex interactions and feedback processes between deep-water circulation, stagnation/stratification and eutrophication for driving deoxygenation dynamics. The rapid deoxygenation of the eastern Mediterranean around 10 ka BP following widespread eutrophication of surface waters, after thousands of years of deep-water stagnation, also calls

https://doi.org/10.5194/cp-2020-114
Preprint. Discussion started: 2 October 2020


Climate of the Past Discussions

for modelling experiments to include nutrient loading as a forcing factor, since it is presently rising due to fertilizer use in the Nile valley (Nixon, 2003; Powley et al., 2016).

6 Conclusions

By combining microfacies analyses with downcore geochemical measurements, our study provides a first estimation of changes in oxygenation conditions of the bottom waters off the western mouth of the Nile River in the eastern Mediterranean. The regular seasonal alternation of detrital, biogenic and chemical sublayers in the laminated sequence deposited during sapropel S1 in a set of cores from different water depths on the western Nile deep-sea fan are interpreted in terms of seasonal changes (Fig. 5c). Strong summer Nile floods during S1 led to the deposition of thick (up to a few mm) silt-sized detrital sublayers that dominate total layer thickness. The deposits of our study thus confirm the large influence of Nile runoff on the eastern Mediterranean realm during sapropel deposition. The large floods triggered surface blooms of planktonic foraminifera and coccoliths in autumn, which are similar to historical "Nile blooms" described during the last natural flood of the Nile River (Halim et al., 1967). The subsequent deposition of clay-rich detrital sublayers was associated with the low discharge regime of the Nile during winter. The occurrence of inorganic carbonate sublayers in several laminated cores from the western Nile deep-sea fan suggests that bottom waters reached a supersaturation state for calcite. The depleted $\delta^{13}C$ signature of these sublayers points to the existence of anoxic to euxinic (and sometimes methane-rich) bottom waters above the fan accompanied by a high level of anaerobic remineralisation of organic matter leading to high alkalinity. The most likely process initiating the deposition of these layers was the onset of the strong Nile floods as a consequence of increased precipitation, which supplied sufficient amounts of cations to the seawater. Our pilot measurements on the sub-millimetre layers underpin their potential to reconstruct seawater chemistry at times when no benthic fauna existed.

On millennial time-scales, we show that variations in oxygenation dynamics followed changes in primary productivity driven by nutrient fertilisation during high Nile runoff. Deoxygenation above the fan shoaled to water depths as shallow as 400 m offshore the Nile mouth and varied on centennial- to millennial-scales in the upper 750 m water depth. In contrast, the records of the cores located below 1000 m water-depth reflect more stable anoxic conditions between 10 and 6.5 ka BP. The development and fluctuations of anoxic conditions during sapropel S1 are coherent regionally and therefore suggest a common control. Even though multi-millennial development of deep-water stagnation was posited as a necessary prerequisite to basin-scale anoxia in the eastern Mediterranean (Cornuault et al., 2018; Grimm et al., 2015), our records and data compilation show that changes in primary productivity in the surface drove the rapid changes in oxygenation state through eutrophication processes. Indeed,

https://doi.org/10.5194/cp-2020-114
Preprint. Discussion started: 2 October 2020


Climate of the Past Discussions

718 tight temporal links between regional productivity records, oxygenation and runoff dynamics, as well as the
719 evidence of stronger deoxygenation close to the Nile mouth point to a pivotal role of runoff-driven fertilisation.
720 Furthermore, the rapid switch towards anoxic conditions around 10 ka BP suggests the existence of thresholds or
721 tipping points, which still remain elusive. Such processes should be further explored using modelling experiments
722 incorporating new boundary conditions, such as nutrient loading from Nile runoff, either for forecasting future
723 deoxygenation dynamics or for understanding feedback processes in the past.

724 **Data availability**

725 All data presented in this paper will be available at PANGEA upon publication of the paper and for the reviewers
726 Table S1: Elemental contents measured by XRF for core P362/2-33 and shown in Fig. 2, 6, 8 and 9.
727 Table S2: Elemental contents measured by XRF for core P362/2-99 and shown in Fig. 2, 6, 8 and 9.
728 Table S3: Elemental contents measured by XRF for core P362/2-73 and shown in Fig. 2, 6, 8 and 9.
729 Table S4: Oxygen and carbon isotope data for core P362/2-33 shown in Fig. 4.
730 Table S5: Biomarker data for core P362/2-33 shown in Fig. 6, 7, 8 and 9.
731 Table S6: Biomarker data for core P362/2-99 shown in Fig. 6, 7, 8 and 9.

732 **Supplement Link**

733 For the present submission, supplementary figures are provided in a separate file.

734 **Author contribution**

735 CLB designed the study, measured and analysed the data. RT measured and analysed the XRF elemental contents.
736 AES assisted with XRD measurements. SS, MF and AB provided guidance, lab space and logistic support for
737 biomarker measurements, sedimentology and micro-facies analyses, respectively. CLB wrote the manuscript, to
738 which all co-authors contributed.

739 **Competing interests**

740 The authors declare that they have no conflicts of interest.

741 **Acknowledgements**

742 Measurements for this paper were carried out during a DFG own-position grant to C.B. at GEOMAR (Kiel,
743 Germany) and NIOZ (Texel, Netherlands) (BL2111/1-1, 2010-2013) and during a reintegration grant at GFZ

https://doi.org/10.5194/cp-2020-114
Preprint. Discussion started: 2 October 2020

(Potsdam, Germany) (2018-2020). We are grateful to our colleagues from section 4.3 at GFZ for their support in term of sample preparation (B. Brademann), measurements (Stable isotopes lab, B. Plessen and S. Pinkerneil) and discussions (esp. J. Mingram). We also acknowledge G. Ménot, M. Mojtahid, R. Hennekam and A.Matthews who kindly provided and discussed their data. Paper written during the lockdown due to COVID-19 (March to June 2020) with background support from Daniel Hope and Max Richter.

References

Abu-Zied, R. H., Rohling, E. J., Jorissen, F. J., Fontanier, C., Casford, J. S. L. and Cooke, S.: Benthic foraminiferal response to changes in bottom-water oxygenation and organic carbon flux in the eastern Mediterranean during LGM to Recent times, Mar. Micropaleontol., 67(1–2), 46–68, doi:10.1016/j.marmicro.2007.08.006, 2008.

Aloisi, G., Pierre, C., Rouchy, J.-M., Foucher, J.-P. and Woodside, J.: Methane-related authigenic carbonates of eastern Mediterranean Sea mud volcanoes and their possible relation to gas hydrate destabilisation, Earth Planet. Sci. Lett., 184(1), 321–338, doi:10.1016/S0012-821X(00)00322-8, 2000.

Aloisi, G., Bouloubassi, I., Heijs, S. K., Pancost, R. D., Pierre, C., Sinninghe Damsté, J. S., Gottschal, J. C., Forney, L. J. and Rouchy, J.-M.: CH4-consuming microorganisms and the formation of carbonate crusts at cold seeps, Earth Planet. Sci. Lett., 203(1), 195–203, doi:10.1016/S0012-821X(02)00878-6, 2002.

Azrieli-Tal, I., Matthews, A., Bar-Matthews, M., Almogi-Labin, A., Vance, D., Archer, C. and Teutsch, N.: Evidence from molybdenum and iron isotopes and molybdenum–uranium covariation for sulphidic bottom waters during Eastern Mediterranean sapropel S1 formation, Earth Planet. Sci. Lett., 393, 231–242, doi:10.1016/j.epsl.2014.02.054, 2014.

Bayon, G., Dupré, S., Ponzevera, E., Etoubleau, J., Chéron, S., Pierre, C., Mascle, J., Boetius, A. and de Lange, G. J.: Formation of carbonate chimneys in the Mediterranean Sea linked to deep-water oxygen depletion, Nat. Geosci., 6(9), 755–760, doi:10.1038/ngeo1888, 2013.

Benkovitz, A., Matthews, A., Teutsch, N., Poulton, S., Bar-Matthews, M. and Almogi-Labin, A.: Tracing water column euxinia in Eastern Mediterranean Sapropels S5 and S7, Chem. Geol., 119627, doi:10.1016/j.chemgeo.2020.119627, 2020.

Besseling, M. A., Hopmans, E. C., Koenen, M., van der Meer, M. T. J., Vreugdenhil, S., Schouten, S., Sinninghe Damsté, J. S. and Villanueva, L.: Depth-related differences in archaeal populations impact the isoprenoid tetraether lipid composition of the Mediterranean Sea water column, Org. Geochem., 135, 16–31, doi:10.1016/j.orggeochem.2019.06.008, 2019.

Bianchi, D., Zavatarelli, M., Pinardi, N., Capozzi, R., Capotondi, L., Corselli, C. and Masina, S.: Simulations of ecosystem response during the sapropel S1 deposition event, Palaeogeogr. Palaeoclimatol. Palaeoecol., 235(1–3), 265–287, doi:10.1016/j.palaeo.2005.09.032, 2006.

https://doi.org/10.5194/cp-2020-114
Preprint. Discussion started: 2 October 2020

777 Billi, P. and el Badri Ali, O.: Sediment transport of the Blue Nile at Khartoum, Quat. Int., 226(1–2), 12–22,
778 doi:10.1016/j.quaint.2009.11.041, 2010.

779 Blaauw, M. and Christen, J. A.: Flexible paleoclimate age-depth models using an autoregressive gamma process,
780 Bayesian Anal., 6(3), 457–474, doi:10.1214/11-BA618, 2011.

781 Blanchet, C. L., Tjallingii, R., Frank, M., Lorenzen, J., Reitz, A., Brown, K., Feseker, T. and Brückmann, W.:
782 High- and low-latitude forcing of the Nile River regime during the Holocene inferred from laminated sediments of
783 the Nile deep-sea fan, Earth Planet. Sci. Lett., 364, 98–110, doi:10.1016/j.epsl.2013.01.009, 2013.

784 Blanchet, C. L., Frank, M. and Schouten, S.: Asynchronous Changes in Vegetation, Runoff and Erosion in the Nile
785 River Watershed during the Holocene, PLOS ONE, 9(12), e115958, doi:10.1371/journal.pone.0115958, 2014.

786 Brauer, A. and Casanova, J.: Chronology and depositional processes of the laminated sediment record from Lac
787 d'Annecy, French Alps, J. Paleolimnol., 25(2), 163–177, doi:10.1023/A:1008136029735, 2001.

788 Bray, E. E. and Evans, E. D.: Distribution of n-paraffins as a clue to recognition of source beds, Geochim.
789 Cosmochim. Acta, 22(1), 2–15, doi:10.1016/0016-7037(61)90069-2, 1961.

790 Brooks, S. P. and Gelman, A.: General Methods for Monitoring Convergence of Iterative Simulations, J. Comput.
791 Graph. Stat., 7(4), 434–455, doi:10.1080/10618600.1998.10474787, 1998.

792 Castañeda, I., Schefuß, E., Pätzold, J., Sinninghe Damsté, J. S., Weldeab, S. and Schouten, S.: Millennial-scale sea
793 surface temperature changes in the eastern Mediterranean (Nile River Delta region) over the last 27,000 years,
794 Paleoceanography, 25(1), doi:10.1029/2009PA001740, 2010.

795 Castañeda, I. S., Schouten, S., Pätzold, J., Lucassen, F., Kasemann, S., Kuhlmann, H. and Schefuß, E.:
796 Hydroclimate variability in the Nile River Basin during the past 28,000 years, Earth Planet. Sci. Lett., 438, 47–56,
797 doi:10.1016/j.epsl.2015.12.014, 2016.

798 Cornuault, M., Tachikawa, K., Vidal, L., Guihou, A., Siani, G., Deschamps, P., Bassinot, F. and Revel, M.:
799 Circulation Changes in the Eastern Mediterranean Sea Over the Past 23,000 Years Inferred From Authigenic Nd
800 Isotopic Ratios, Paleoceanogr. Paleoclimatology, 33(3), 264–280, doi:10.1002/2017PA003227, 2018.

801 Cramp, A. and O'Sullivan, G.: Neogene sapropels in the Mediterranean: a review, Mar. Geol., 153(1), 11–28,
802 doi:10.1016/S0025-3227(98)00092-9, 1999.

803 De Jonge, C., Hopmans, E. C., Zell, C. I., Kim, J.-H., Schouten, S. and Sinninghe Damsté, J. S.: Occurrence and
804 abundance of 6-methyl branched glycerol dialkyl glycerol tetraethers in soils: Implications for palaeoclimate
805 reconstruction, Geochim. Cosmochim. Acta, 141, 97–112, doi:10.1016/j.gca.2014.06.013, 2014.

806 De Lange, G. J., Thomson, J., Reitz, A., Slomp, C. P., Speranza Principato, M., Erba, E. and Corselli, C.:
807 Synchronous basin-wide formation and redox-controlled preservation of a Mediterranean sapropel, Nat. Geosci.,
808 1(9), 606–610, doi:10.1038/ngeo283, 2008.

809 Dekov, V. M., Komy, Z., Araújo, F., Van Put, A. and Van Grieken, R.: Chemical composition of sediments,
810 suspended matter, river water and ground water of the Nile (Aswan-Sohag traverse), Sci. Total Environ., 201(3),
811 195–210, doi:10.1016/S0048-9697(97)84057-0, 1997.

812 Diefendorf, A. F., Freeman, K. H. and Wing, S. L.: Distribution and carbon isotope patterns of diterpenoids and
813 triterpenoids in modern temperate C3 trees and their geochemical significance, Geochim. Cosmochim. Acta, 85,
814 342–356, doi:10.1016/j.gca.2012.02.016, 2012.

815 Ducassou, E., Mulder, T., Migeon, S., Gonthier, E., Murat, A., Revel, M., Capotondi, L., Bernasconi, S. M., Mascle,
816 J. and Zaragosi, S.: Nile floods recorded in deep Mediterranean sediments, Quat. Res., 70(03), 382–391,
817 doi:10.1016/j.yqres.2008.02.011, 2008.

818 Feseker, T., Brown, K. R., Blanchet, C., Scholz, F., Nuzzo, M., Reitz, A., Schmidt, M. and Hensen, C.: Active mud
819 volcanoes on the upper slope of the western Nile deep-sea fan—first results from the P362/2 cruise of R/V
820 Poseidon, Geo-Mar. Lett., 30(3–4), 169–186, doi:10.1007/s00367-010-0192-0, 2010.

821 Fry, B., Jannasch, H. W., Molyneaux, S. J., Wirsen, C. O., Muramoto, J. A. and King, S.: Stable isotope studies of
822 the carbon, nitrogen and sulfur cycles in the Black Sea and the Cariaco Trench, Deep Sea Res. Part Oceanogr. Res.
823 Pap., 38, S1003–S1019, doi:10.1016/S0198-0149(10)80021-4, 1991.

824 Ganopolski, A. and Rahmstorf, S.: Rapid changes of glacial climate simulated in a coupled climate model, Nature,
825 409(6817), 153–158, 2001.

826 Garzanti, E., Andò, S., Vezzoli, G., Ali Abdel Megid, A. and El Kammar, A.: Petrology of Nile River sands
827 (Ethiopia and Sudan): Sediment budgets and erosion patterns, Earth Planet. Sci. Lett., 252(3–4), 327–341,
828 doi:10.1016/j.epsl.2006.10.001, 2006.

829 Garzanti, E., Andò, S., Padoan, M., Vezzoli, G. and El Kammar, A.: The modern Nile sediment system: Processes
830 and products, Quat. Sci. Rev., 130, 9–56, doi:10.1016/j.quascirev.2015.07.011, 2015.

831 Garzanti, E., Vermeesch, P., Rittner, M. and Simmons, M.: The zircon story of the Nile: Time-structure maps of
832 source rocks and discontinuous propagation of detrital signals, Basin Res., 30(6), 1098–1117,
833 doi:10.1111/bre.12293, 2018.

834 Gebco team: Gebco, Gebco Gen. Bathymetr. Chart Ocean [online] Available from: https://www.gebco.net/, 2014.

835 Goudie, A. S. and Middleton, N. J.: Saharan dust storms: nature and consequences, Earth-Sci. Rev., 56(1–4), 179–
836 204, doi:10.1016/S0012-8252(01)00067-8, 2001.

837 Grimm, R., Maier-Reimer, E., Mikolajewicz, U., Schmiedl, G., Müller-Navarra, K., Adloff, F., Grant, K. M.,
838 Ziegler, M., Lourens, L. J. and Emeis, K.-C.: Late glacial initiation of Holocene eastern Mediterranean sapropel
839 formation, Nat. Commun., 6, 7099, doi:10.1038/ncomms8099, 2015.

840 Halim, Y., Guergues, S. K. and Saleh, H. H.: Hydrographic Conditions and Plankton in the South East
841 Mediterranean During the Last Normal Nile Flood (1964), Int. Rev. Gesamten Hydrobiol. Hydrogr., 52(3), 401–
842 425, doi:10.1002/iroh.19670520305, 1967.

https://doi.org/10.5194/cp-2020-114
Preprint. Discussion started: 2 October 2020

Hennekam, R., Jilbert, T., Schnetger, B. and de Lange, G. J.: Solar forcing of Nile discharge and sapropel S1 formation in the early to middle Holocene eastern Mediterranean, Paleoceanography, 29(5), 343–356, doi:10.1002/2013PA002553, 2014.

Hennekam, R., Donders, T. H., Zwiep, K. and de Lange, G. J.: Integral view of Holocene precipitation and vegetation changes in the Nile catchment area as inferred from its delta sediments, Quat. Sci. Rev., 130, 189–199, doi:10.1016/j.quascirev.2015.05.031, 2015.

Hopmans, E. C., Weijers, J. W. H., Schefuß, E., Herfort, L., Sinninghe Damsté, J. S. and Schouten, S.: A novel proxy for terrestrial organic matter in sediments based on branched and isoprenoid tetraether lipids, Earth Planet. Sci. Lett., 224(1–2), 107–116, doi:10.1016/j.epsl.2004.05.012, 2004.

Jacob, J., Disnar, J.-R., Boussafir, M., Spadano Albuquerque, A. L., Sifeddine, A. and Turcq, B.: Pentacyclic triterpene methyl ethers in recent lacustrine sediments (Lagoa do Caçò, Brazil), Org. Geochem., 36(3), 449–461, doi:10.1016/j.orggeochem.2004.09.005, 2005.

Jilbert, T. and Slomp, C. P.: Iron and manganese shuttles control the formation of authigenic phosphorus minerals in the euxinic basins of the Baltic Sea, Geochim. Cosmochim. Acta, 107, 155–169, doi:10.1016/j.gca.2013.01.005, 2013.

Jorissen, F. J.: Benthic foraminiferal successions across Late Quaternary Mediterranean sapropels, Mar. Geol., 153(1), 91–101, 1999.

Kemp, A. E., Pearce, R. B., Koizumi, I., Pike, J. and Rance, S. J.: The role of mat-forming diatoms in the formation of Mediterranean sapropels, Nature, 398(6722), 57, 1999.

Krom, M. D., Kress, N. and Fanning, K.: Silica cycling in the ultra-oligotrophic eastern Mediterranean Sea, Biogeosciences, 11(15), 4211–4223, doi:10.5194/bg-11-4211-2014, 2014.

Kuhnt, T., Schmiedl, G., Ehrmann, W., Hamann, Y. and Andersen, N.: Stable isotopic composition of Holocene benthic foraminifers from the Eastern Mediterranean Sea: Past changes in productivity and deep water oxygenation, Palaeogeogr. Palaeoclimatol. Palaeoecol., 268(1–2), 106–115, doi:10.1016/j.palaeo.2008.07.010, 2008.

Larrasoaña, J. C., Roberts, A. P., Hayes, A., Wehausen, R. and Rohling, E. J.: Detecting missing beats in the Mediterranean climate rhythm from magnetic identification of oxidized sapropels (Ocean Drilling Program Leg 160), Phys. Earth Planet. Inter., 156(3–4), 283–293, doi:10.1016/j.pepi.2005.04.017, 2006.

Le Houedec, S., Mojtahid, M., Bicchi, E., Lange, G. J. de and Hennekam, R.: Suborbital Hydrological Variability Inferred From Coupled Benthic and Planktic Foraminiferal-Based Proxies in the Southeastern Mediterranean During the Last 19 ka, Paleoceanogr. Paleoclimatology, 35(2), e2019PA003827, doi:10.1029/2019PA003827, 2020.

Liu, Q., Larrasoaña, J. C., Torrent, J., Roberts, A. P., Rohling, E. J., Liu, Z. and Jiang, Z.: New constraints on climate forcing and variability in the circum-Mediterranean region from magnetic and geochemical observations of sapropels S1, S5 and S6, Palaeogeogr. Palaeoclimatol. Palaeoecol., 333–334, 1–12, doi:10.1016/j.palaeo.2012.02.036, 2012.

https://doi.org/10.5194/cp-2020-114
Preprint. Discussion started: 2 October 2020

878 Marlowe, I. T., Green, J. C., Neal, A. C., Brassell, S. C., Eglinton, G. and Course, P. A.: Long chain (n-C37–C39)
879 alkenones in the Prymnesiophyceae. Distribution of alkenones and other lipids and their taxonomic significance,
880 Br. Phycol. J., 19(3), 203–216, doi:10.1080/00071618400650221, 1984.

881 Matthews, A., Azrieli-Tal, I., Benkovitz, A., Bar-Matthews, M., Vance, D., Poulton, S. W., Teutsch, N., Almogi-
882 Labin, A. and Archer, C.: Anoxic development of sapropel S1 in the Nile Fan inferred from redox sensitive proxies,
883 Fe speciation, Fe and Mo isotopes, Chem. Geol., 475, 24–39, doi:10.1016/j.chemgeo.2017.10.028, 2017.

884 MEDAR Group: MEDATLAS/2002 database. Mediterranean and Black Sea database of temperature salinity and
885 bio-chemical parameters. Climatological Atlas. (4 CD-Roms), [online] Available from:
886 http://www.ifremer.fr/medar/cdrom_database.htm, 2002.

887 Ménot, G., Pivot, S., Bouloubassi, I., Davtian, N., Hennekam, R., Bosch, D., Ducassou, E., Bard, E., Migeon, S.
888 and Revel, M.: Timing and stepwise transitions of the African Humid Period from geochemical proxies in the Nile
889 deep-sea fan sediments, Quat. Sci. Rev., 228, 106071, doi:10.1016/j.quascirev.2019.106071, 2020.

890 Michaelis, W., Seifert, R., Nauhaus, K., Treude, T., Thiel, V., Blumenberg, M., Knittel, K., Gieseke, A.,
891 Peterknecht, K., Pape, T., Boetius, A., Amann, R., Jørgensen, B. B., Widdel, F., Peckmann, J., Pimenov, N. V. and
892 Gulin, M. B.: Microbial Reefs in the Black Sea Fueled by Anaerobic Oxidation of Methane, Science, 297(5583),
893 1013–1015, doi:10.1126/science.1072502, 2002.

894 Mojtahid, M., Manceau, R., Schiebel, R., Hennekam, R. and de Lange, G. J.: Thirteen thousand years of
895 southeastern Mediterranean climate variability inferred from an integrative planktic foraminiferal-based approach,
896 Paleoceanography, 30(4), 402–422, doi:10.1002/2014PA002705, 2015.

897 Mologni, C., Revel, M., Blanchet, C., Bosch, D., Develle, A.-L., Orange, F., Bastian, L., Khalidi, L., Ducassou, E.
898 and Migeon, S.: Frequency of exceptional Nile flood events as an indicator of Holocene hydroclimatic changes in
899 the Ethiopian Highlands, Quat. Sci. Rev., in press.

900 Nägler, T. F., Neubert, N., Böttcher, M. E., Dellwig, O. and Schnetger, B.: Molybdenum isotope fractionation in
901 pelagic euxinia: Evidence from the modern Black and Baltic Seas, Chem. Geol., 289(1), 1–11,
902 doi:10.1016/j.chemgeo.2011.07.001, 2011.

903 Nixon, S. W.: Replacing the Nile: Are Anthropogenic Nutrients Providing the Fertility Once Brought to the
904 Mediterranean by a Great River?, AMBIO J. Hum. Environ., 32(1), 30–39, doi:10.1579/0044-7447-32.1.30, 2003.

905 Oschlies, A., Dietze, H. and Kähler, P.: Salt-finger driven enhancement of upper ocean nutrient supply, Geophys.
906 Res. Lett., 30(23), doi:10.1029/2003GL018552, 2003.

907 Pante, E. and Simon-Bouhet, B.: marmap: A Package for Importing, Plotting and Analyzing Bathymetric and
908 Topographic Data in R, PLOS ONE, 8(9), e73051, doi:10.1371/journal.pone.0073051, 2013.

909 Parsons, J. D., Bush, J. W. M. and Syvitski, J. P. M.: Hyperpycnal plume formation from riverine outflows with
910 small sediment concentrations, Sedimentology, 48(2), 465–478, doi:10.1046/j.1365-3091.2001.00384.x, 2001.

https://doi.org/10.5194/cp-2020-114
Preprint. Discussion started: 2 October 2020

Pinardi, N., Zavatarelli, M., Adani, M., Coppini, G., Fratianni, C., Oddo, P., Simoncelli, S., Tonani, M., Lyubartsev, V., Dobricic, S. and Bonaduce, A.: Mediterranean Sea large-scale low-frequency ocean variability and water mass formation rates from 1987 to 2007: A retrospective analysis, Prog. Oceanogr., 132, 318–332, doi:10.1016/j.pocean.2013.11.003, 2015.

Powley, H. R., Krom, M. D. and Van Cappellen, P.: Circulation and oxygen cycling in the Mediterranean Sea: Sensitivity to future climate change, J. Geophys. Res. Oceans, 121, 8230–8247, 2016.

R Core Team: R: A language and environment for statistical computing, R Foundation for Statistical Computing, Vienna, Austria. [online] Available from: http://www.R-project.org/, 2013.

Revel, M., Ducassou, E., Skonieczny, C., Colin, C., Bastian, L., Bosch, D., Migeon, S. and Mascle, J.: 20,000 years of Nile River dynamics and environmental changes in the Nile catchment area as inferred from Nile upper continental slope sediments, Quat. Sci. Rev., 130, 200–221, doi:10.1016/j.quascirev.2015.10.030, 2015.

Riedinger, N., Brunner, B., Lin, Y.-S., Voßmeyer, A., Ferdelman, T. G. and Jørgensen, B. B.: Methane at the sediment–water transition in Black Sea sediments, Chem. Geol., 274(1), 29–37, doi:10.1016/j.chemgeo.2010.03.010, 2010.

Robinson, A. R., Malanotte-Rizzoli, P., Hecht, A., Michelato, A., Roether, W., Theocharis, A., Ünlüata, Ü., Pinardi, N., Artegiani, A., Bergamasco, A., Bishop, J., Brenner, S., Christianidis, S., Gacic, M., Georgopoulos, D., Golnaraghi, M., Hausmann, M., Junghaus, H.-G., Lascaratos, A., Latif, M. A., Leslie, W. G., Lozano, C. J., Og˛uz, T., Özsoy, E., Papageorgiou, E., Paschini, E., Rozentroub, Z., Sansone, E., Scarazzato, P., Schlitzer, R., Spezie, G.-C., Tziperman, E., Zodiatis, G., Athanassiadou, L., Gerges, M. and Osman, M.: General circulation of the Eastern Mediterranean, Earth-Sci. Rev., 32(4), 285–309, doi:10.1016/0012-8252(92)90002-B, 1992.

Roether, W., Manca, B. B., Klein, B., Bregant, D., Georgopoulos, D., Beitzel, V., Kovačević, V. and Luchetta, A.: Recent Changes in Eastern Mediterranean Deep Waters, Science, 271(5247), 333–335, doi:10.1126/science.271.5247.333, 1996.

Roether, W., Klein, B., Manca, B. B., Theocharis, A. and Kioroglou, S.: Transient Eastern Mediterranean deep waters in response to the massive dense-water output of the Aegean Sea in the 1990s, Prog. Oceanogr., 74(4), 540–571, doi:10.1016/j.pocean.2007.03.001, 2007.

Rogerson, M., Colmenero-Hidalgo, E., Levine, R. C., Rohling, E. J., Voelker, A. H. L., Bigg, G. R., Schönfeld, J., Cacho, I., Sierro, F. J., Löwemark, L., Reguera, M. I., Abreu, L. de and Garrick, K.: Enhanced Mediterranean-Atlantic exchange during Atlantic freshening phases, Geochem. Geophys. Geosystems, 11(8), doi:10.1029/2009GC002931, 2010.

Rogerson, M., Rohling, E. J., Bigg, G. R. and Ramirez, J.: Paleoceanography of the Atlantic-Mediterranean exchange: Overview and first quantitative assessment of climatic forcing, Rev. Geophys., 50(2), doi:10.1029/2011RG000376, 2012.

Rohling, E. J.: Review and new aspects concerning the formation of eastern Mediterranean sapropels, Mar. Geol., 122(1), 1–28, doi:10.1016/0025-3227(94)90202-X, 1994.

https://doi.org/10.5194/cp-2020-114
Preprint. Discussion started: 2 October 2020

946 Rohling, E. J., Hopmans, E. C. and Damsté, J. S. S.: Water column dynamics during the last interglacial anoxic
947 event in the Mediterranean (sapropel S5), Paleoceanography, 21(2), doi:10.1029/2005PA001237, 2006.

948 Rohling, E. J., Marino, G. and Grant, K. M.: Mediterranean climate and oceanography, and the periodic
949 development of anoxic events (sapropels), Earth-Sci. Rev., 143, 62–97, doi:10.1016/j.earscirev.2015.01.008, 2015.

950 Rossignol-Strick, M.: Mediterranean Quaternary sapropels, an immediate response of the African monsoon to
951 variation of insolation, Palaeogeogr. Palaeoclimatol. Palaeoecol., 49(3–4), 237–263, doi:10.1016/0031-
952 0182(85)90056-2, 1985.

953 Rossignol-Strick, M., Nesteroff, W., Olive, P. and Vergnaud-Grazzini, C.: After the deluge: Mediterranean
954 stagnation and sapropel formation, Nature, 295(5845), 105–110, doi:10.1038/295105a0, 1982.

955 Rush, D., Talbot, H. M., Meer, M. T. J. van der, Hopmans, E. C., Douglas, B. and Sinninghe Damsté, J. S.:
956 Biomarker evidence for the occurrence of anaerobic ammonium oxidation in the eastern Mediterranean Sea during
957 Quaternary and Pliocene sapropel formation, Biogeosciences, 16(12), 2467–2479, doi:https://doi.org/10.5194/bg-
958 16-2467-2019, 2019.

959 Rutten, A. and de Lange, G. J.: Sequential extraction of iron, manganese and related elements in S1 sapropel
960 sediments, eastern Mediterranean, Palaeogeogr. Palaeoclimatol. Palaeoecol., 190, 79–101, doi:10.1016/S0031-
961 0182(02)00600-4, 2003.

962 Schimmelmann, A., Lange, C. B., Schieber, J., Francus, P., Ojala, A. E. K. and Zolitschka, B.: Varves in marine
963 sediments: A review, Earth-Sci. Rev., 159, 215–246, doi:10.1016/j.earscirev.2016.04.009, 2016.

964 Schlitzer, R.: Ocean Data View, Alfred-Wegener Institute AWI Bremerhaven. [online] Available from: odv.awi.de,
965 2018.

966 Schmiedl, G., Mitschele, A., Beck, S., Emeis, K.-C., Hemleben, C., Schulz, H., Sperling, M. and Weldeab, S.:
967 Benthic foraminiferal record of ecosystem variability in the eastern Mediterranean Sea during times of sapropel S5
968 and S6 deposition, Palaeogeogr. Palaeoclimatol. Palaeoecol., 190, 139–164, doi:10.1016/S0031-0182(02)00603-
969 X, 2003.

970 Schmiedl, G., Kuhnt, T., Ehrmann, W., Emeis, K.-C., Hamann, Y., Kotthoff, U., Dulski, P. and Pross, J.: Climatic
971 forcing of eastern Mediterranean deep-water formation and benthic ecosystems during the past 22?000 years, Quat.
972 Sci. Rev., 29(23–24), 3006–3020, doi:10.1016/j.quascirev.2010.07.002, 2010.

973 Schouten, S., Wakeham, S. G. and Damsté, J. S. S.: Evidence for anaerobic methane oxidation by archaea in euxinic
974 waters of the Black Sea, Org. Geochem., 32(10), 1277–1281, doi:10.1016/S0146-6380(01)00110-3, 2001.

975 Schouten, S., Huguet, C., Hopmans, E. C., Kienhuis, M. V. M. and Sinninghe Damst?, J. S.: Analytical
976 Methodology for TEX $_{86}$ Paleothermometry by High-Performance Liquid Chromatography/Atmospheric Pressure
977 Chemical Ionization-Mass Spectrometry, Anal. Chem., 79(7), 2940–2944, doi:10.1021/ac062339v, 2007.

978 Sinninghe Damsté, J. S.: Spatial heterogeneity of sources of branched tetraethers in shelf systems: The
979 geochemistry of tetraethers in the Berau River delta (Kalimantan, Indonesia), Geochim. Cosmochim. Acta, 186,
980 13–31, doi:10.1016/j.gca.2016.04.033, 2016.

981 Sinninghe Damsté, J. S., Kuypers, M. M. M., Schouten, S., Schulte, S. and Rullkötter, J.: The lycopane/C31 n-
982 alkane ratio as a proxy to assess palaeoxicity during sediment deposition, Earth Planet. Sci. Lett., 209(1–2), 215–
983 226, doi:10.1016/S0012-821X(03)00066-9, 2003.

984 Somot, S., Houpert, L., Sevault, F., Testor, P., Bosse, A., Taupier-Letage, I., Bouin, M.-N., Waldman, R., Cassou,
985 C., Sanchez-Gomez, E., Durrieu de Madron, X., Adloff, F., Nabat, P. and Herrmann, M.: Characterizing, modelling
986 and understanding the climate variability of the deep water formation in the North-Western Mediterranean Sea,
987 Clim. Dyn., 51(3), 1179–1210, doi:10.1007/s00382-016-3295-0, 2018.

988 Tachikawa, K., Vidal, L., Cornuault, M., Garcia, M., Pothin, A., Sonzogni, C., Bard, E., Menot, G. and Revel, M.:
989 Eastern Mediterranean Sea circulation inferred from the conditions of S1 sapropel deposition, Clim. Past, 11, 855–
990 867, 2015.

991 Tang, C. M. and Stott, L. D.: Seasonal salinity changes during Mediterranean sapropel deposition 9000 years B.P.:
992 Evidence from isotopic analyses of individual planktonic foraminifera, Paleoceanography, 8(4), 473–493,
993 doi:10.1029/93PA01319, 1993.

994 Volkman, J. K.: Ecological and environmental factors affecting alkenone distributions in seawater and sediments,
995 Geochem. Geophys. Geosystems, 1(9), doi:10.1029/2000GC000061, 2000.

996 Weldeab, S., Menke, V. and Schmiedl, G.: The pace of East African monsoon evolution during the Holocene,
997 Geophys. Res. Lett., 41(5), 1724–1732, doi:10.1002/2014GL059361, 2014.

998 Weltje, G. J. and Tjallingii, R.: Calibration of XRF core scanners for quantitative geochemical logging of sediment
999 cores: Theory and application, Earth Planet. Sci. Lett., 274(3–4), 423–438, doi:10.1016/j.epsl.2008.07.054, 2008.

000 Weltje, G. J., Bloemsma, M. R., Tjallingii, R., Heslop, D., Röhl, U. and Croudace, I. W.: Prediction of Geochemical
001 Composition from XRF Core Scanner Data: A New Multivariate Approach Including Automatic Selection of
002 Calibration Samples and Quantification of Uncertainties, in Micro-XRF Studies of Sediment Cores, vol. 17, edited
003 by I. W. Croudace and R. G. Rothwell, pp. 507–534, Springer Netherlands, Dordrecht., 2015.

004 Xiao, W., Wang, Y., Zhou, S., Hu, L., Yang, H. and Xu, Y.: Ubiquitous production of branched glycerol dialkyl
005 glycerol tetraethers (brGDGTs) in global marine environments: a new source indicator for brGDGTs,
006 Biogeosciences, 13(20), 5883–5894, doi:https://doi.org/10.5194/bg-13-5883-2016, 2016.

007 Zirks, E., Krom, M. D., Zhu, D., Schmiedl, G. and Goodman-Tchernov, B. N.: Evidence for the Presence of
008 Oxygen-Depleted Sapropel Intermediate Water across the Eastern Mediterranean during Sapropel S1, ACS Earth
009 Space Chem., doi:10.1021/acsearthspacechem.9b00128, 2019.

010

011